

Rf Dressing of Rydberg States in Hollow-Core Fibers

Masterarbeit
Christian Veit
Stuttgart, 24. März 2015

Hauptberichter: Prof. Dr. Tilman Pfau
Mitberichter: Prof. Dr. Martin Dressel

Universität Stuttgart
5. Physikalisches Institut

Erklärung

Hiermit erkläre ich, dass ich diese Arbeit selbständig verfasst und keine anderen als die von mir angegebenen Quellen und Hilfsmittel verwendet habe.

Stuttgart, den 24. März 2015

Christian Veit

Abstract

This thesis reports on a spectroscopic study of Rydberg atoms inside cesium vapor-filled hollow-core fibers. The experimental apparatus designed and built in the scope of this work allows for the application of radio-frequency (rf) electric fields to individual segments along a fiber. This setup was employed to gain a spatial resolution of the spectroscopy signal along the fiber and to study the formation of rf-induced sidebands in the spectra. The experimental results obtained in this context are discussed and explained theoretically. Furthermore, simulations of the three-photon Rydberg excitation scheme are presented and the diffusion of cesium vapor into hollow-core fibers is discussed on the basis of measurement results and a theoretical model.

Zusammenfassung

In dieser Arbeit werden die Ergebnisse einer spektroskopischen Untersuchung von Rydberg Atomen in mit Cäsiumdampf gefüllten Hohlkernfasern vorgestellt. Der experimentelle Aufbau, der im Rahmen dieser Arbeit entworfen und gebaut wurde, erlaubt es hochfrequente elektrische Felder an einzelne Fasersegmente anzulegen. Dies wurde genutzt um eine örtliche Auflösung des Spektroskopiesignals entlang einer Faser zu erzielen und die Formation von Seitenbändern in den Spektren zu untersuchen. Die experimentellen Ergebnisse werden diskutiert und theoretisch erklärt. Weiterhin werden Simulationen des Drei-Photonen-Anregungsschemas vorgestellt und die Diffusion von Cäsium Dampf in Hohlkernfasern hinein anhand von Messergebnissen und einem theoretischen Modell diskutiert.

Contents

1	Introduction	7
2	Theoretical Foundations	9
2.1	Cesium	9
2.2	Rydberg Atoms	9
2.3	Dc Stark Effect	10
2.4	Atom-Light Interaction	11
2.5	Hollow-Core Optical Fibers	15
3	Experimental Apparatus	18
3.1	Vacuum System	18
3.2	CF40-Chamber	18
3.3	E-Chamber	20
3.4	Optical Setup	23
4	Three-Photon Rydberg Spectroscopy	26
4.1	Excitation Scheme	26
4.2	Lineshape of the Three-Photon Signal	27
4.3	Simulations	28
4.4	Spectroscopic Results	32
5	Diffusion of Cesium Vapor into Hollow-Core Fibers	35
5.1	Theoretical Diffusion Model	35
5.2	Experimental Results	38
6	Spectroscopy in Hollow-Core Fibers	42
6.1	Guiding Properties	42
6.2	Spectroscopic Results	42
7	Rf Dressing of the Rydberg State	46
7.1	Theoretical Framework	46
7.2	Electrical Addressing of Fiber Segments	49
7.3	Rf-induced Sidebands of the Rydberg State	54
8	Conclusion and Outlook	59
A	Physical and Atomic Properties of Cs	62
B	Bibliography	64

1 Introduction

The history of modern atomic physics finds its origin in the studies of Niels Bohr who postulated the existence of discrete energy states of atoms in 1913 [1]. His work did not only explain the spectral emission lines of hydrogen but also contributed significantly to the development of quantum mechanics. Nowadays, atomic physics constitutes a many-faceted field of research, reaching from very fundamental aspects like the search for varying fundamental constants [2] to possible future applications, for example in quantum information [3]. With respect to applications, a seemingly trivial property of atoms is especially interesting: all atoms of one kind have the exact same mass, size, energy structure and sensitivity to external fields. It is therefore that atom-based metrology is highly promising and great effort is being made to relate atomic properties to macroscopic quantities. An impressive example of this field are atomic clocks with current instabilities on the order of 10^{-18} [4].

A special class of atoms is represented by highly excited atoms. These so-called Rydberg atoms [5] possess exaggerated properties in comparison to ground state atoms such as high sensitivity to external electric fields and large interaction strengths among themselves. The latter can induce an excitation blockade [6] which has been exploited in ultracold experiments to demonstrate non-classical light [7, 8] and quantum information processing [9]. Recently, Rydberg atoms were employed to realize an all-optical transistor on the single-photon level [10]. Thermal Rydberg atoms have been used to demonstrate coherent Rydberg excitation in microscopic vapor cells [11], to study Rabi oscillations to a Rydberg state in a rubidium vapor [12] and to accurately measure microwave electric fields [13]. These examples show that coherent Rydberg physics is accessible at room temperature and suggest the feasibility of miniaturized Rydberg-based devices such as microwave sensors.

Hollow-core photonic crystal fibers [14] which provide low-loss light guidance in a hollow core paved the way to a new and interesting system: vapor-filled optical waveguides. A major advantage of this system with respect to free space experiments is the large overlap of a single light mode with the atomic ensemble over an effectively unlimited interaction length. Moreover, gas-filled hollow-core fibers provide a platform for miniaturized frequency standards [15, 16] and might be integrated into large scale optical networks due to the possibility to splice them to standard single-mode fibers [15]. Atom-filled hollow-core photonic crystal fibers have been employed in ultracold experiments to realize an all-optical switch [17] and for precision spectroscopy [18]. In room temperature experiments, four-wave mixing [19], electromagnetically induced transparency [20, 21] and an optical memory on the single-photon level [22] was demonstrated. In 2014, Rydberg excitation in hollow-core fibers was reported for fiber diameters down to $19\,\mu\text{m}$ [23, 24]. This achievement is highly promising since it opens up new possibilities for room temperature Rydberg-based applications and constitutes a major step towards the study of quasi-one-dimensional thermal Rydberg vapors.

Within the scope of this thesis, thermal cesium Rydberg atoms in hollow-core fibers were investigated and the action of radio-frequency (rf) electric fields on the atoms was studied.

Rf-dressed Rydberg states have been described in Ref. [25] and were used to phase modulate light [26], to measure atomic polarizabilities [27, 28] and to observe Stückelberg oscillations [29]. Especially interesting with respect to sensing applications is the fact that rf dressing was found to enhance the sensitivity of Rydberg states to electric fields [30]. Due to the large polarizability of Rydberg atoms, already small rf amplitudes on the order of V/cm have profound impact on the behavior of the Rydberg state. Under appropriate conditions, the latter acquires sidebands separated by multiples of the rf frequency. These Floquet states lead to a modulation of the excitation light which in turn also acquires sidebands at multiples of the rf frequency. The studied system of rf-dressed Rydberg states in hollow-core fibers therefore has potential in possible future applications such as low-voltage atom-based fiber modulators.

This thesis is structured in eight chapters. Chapter 2 provides a brief introduction to the theoretical background of the experiment and especially discusses the interaction of atoms with light fields. Chapter 3 gives a detailed description of the experimental setup. Chapter 4 discusses the Rydberg excitation scheme involving two intermediate states. Additionally, simulations of the atomic system are presented and compared to experimental results. Chapter 5 is devoted to the diffusion process of cesium vapor into hollow-core fibers which was studied both experimentally and theoretically. Spectroscopic results obtained with the employed hollow-core fibers are discussed in Ch. 6 and interpreted in the light of previous findings [23, 24]. Rf-dressed Rydberg states are subject of Ch. 7, where both experimental results are presented and a theoretical model is introduced. Subsequently, a conclusion and an outlook are given in Ch. 8.

2 Theoretical Foundations

The focus of this thesis is on the spectroscopy of cesium Rydberg atoms in hollow-core fibers and on the influence of radio-frequency electric fields on Rydberg states. In the following, the theoretical foundations of the described work are introduced. Basic properties of cesium and Rydberg atoms are presented, and the Stark effect describing the action of electric fields on atoms is discussed. The main part of the chapter is devoted to atom-light interaction which is treated on the basis of a semiclassical model. Furthermore, light-guiding hollow-core fibers are subject of the chapter.

2.1 Cesium

Cesium is a silvery-golden metal with a single stable isotope (^{133}Cs). It belongs to the group of the alkali metals in the periodic table, and therefore has one valence electron. Due to their simple electronic structure, cesium and the other stable alkali metals lithium, sodium, potassium and rubidium are often employed in atomic physics. The ground state $6S_{1/2}$ of ^{133}Cs exhibits a hyperfine splitting of (exactly) 9.192 631 77 GHz [31] which provides the basis of the current definition of the second. While cesium is a soft solid at room temperature, it has a very low melting point of 28 °C and a high vapor pressure. For the liquid phase, the latter is approximately given by [31]

$$P_v = 133.322 \text{ Pa} \times 10^{7.046 - \frac{3830 \text{ K}}{T}}, \quad (2.1)$$

where T is the temperature in Kelvin. At room temperature (20 °C), the given expression results in $P_v \approx 1.28 \times 10^{-6} \text{ mbar}$. A vapor pressure curve calculated with Eq. 2.1 is shown in Ch. A. Using the ideal gas law, P_v can be used to estimate the atomic number density of cesium

$$n(T) = \frac{P_v}{k_B T}, \quad (2.2)$$

where k_B is the Boltzmann constant. At 20 °C, this results in a density of $n = 3.2 \times 10^{10} \text{ cm}^{-3}$. Additional physical properties of cesium can be found in Ch. A.

2.2 Rydberg Atoms

An atom is considered a Rydberg atom if one or more of its electrons are in a highly excited state. In the case of cesium, the single valence electron is most loosely bound and can be excited by means of laser excitation to high principal quantum numbers n . The large extent of the electron wave function associated with high principal quantum numbers leads to an extreme sensitivity of Rydberg states to electric fields. Also related to the large orbital size is a hydrogen-like behavior of single electron Rydberg atoms. This behavior arises since the excited electron experiences the Coulomb potential of an effectively singly charged ionic core,

physical property	scaling law
binding energy E_b	n^{*-2}
orbital radius r_{orb}	n^{*2}
radiative lifetime τ	n^{*3}
polarizability α	n^{*7}
VdW coefficient C_6	n^{*11}

Table 2.1: Scaling of selected physical properties of Rydberg atoms with the effective principal quantum number n^* [5, 6]. For this thesis, especially the large polarizability α which scales with n^{*7} is of relevance.

if it is separated sufficiently far from the core. As a consequence, the binding energy can be expressed by the phenomenological formula [5]

$$E_{\text{nlj}} = -\frac{R}{(n - \delta_{\text{nlj}})^2}, \quad (2.3)$$

where R is the Rydberg constant of the considered element (e.g. $R_{\text{Cs}} = hc \times 109\,736.86 \text{ cm}^{-1}$ [5]) and δ_{nlj} is the so-called quantum defect. The latter takes the interaction of the electron with the inner structure of the ionic core into account and depends on the principal quantum number n , the electronic angular momentum l and the total angular momentum j . Commonly, the quantum defect is given in terms of the Rydberg-Ritz coefficients δ_i which are connected to δ_{nlj} by

$$\delta_{\text{nlj}} = \delta_0 + \frac{\delta_2}{(n - \delta_0)^2} + \frac{\delta_4}{(n - \delta_0)^4} + \frac{\delta_6}{(n - \delta_0)^6} \dots \quad (2.4)$$

Rydberg-Ritz coefficients for cesium nS , nP and nD states can be found in Ref. [32]. For the $30P_{3/2}$ Rydberg state, often employed in the described experiment, the coefficients given there result in a quantum defect of $\delta_{30P_{3/2}} = 3.559$. Due to the form of Eq. 2.3, it is useful to define an effective principal quantum number $n^* = n - \delta_{\text{nlj}}$ which can be used to give scaling laws of the physical properties of Rydberg atoms. A selection of such scaling laws is given in Table 2.1.

2.3 Dc Stark Effect

Compared to magnetic fields, electric fields have little influence on ground state atoms because of their small polarizability. Due to the scaling of the polarizability with the effective principal quantum number n^* to the power of seven (see Sec. 2.2), Rydberg atoms however respond highly sensitive to external electric fields. The interaction Hamiltonian of an atom placed into a uniform electric field \mathbf{E} is

$$H_e = -\mathbf{d}\mathbf{E}, \quad (2.5)$$

where \mathbf{d} is the electrical dipole moment of the atom. For small electric fields, H_e can be treated as a perturbation and the energy shift of a specific state can be calculated using perturbation theory. Since the quantum defect lifts the degeneracy of low- l states (see Sec. 2.2), the nP Rydberg states addressed in the described experiment (see Ch. 4) experience a

second order energy shift which is quadratic in E . If the quantization axis is assumed to be parallel to the electric field, this shift is given by [33, 34]

$$\Delta\varepsilon = -\frac{1}{2} \left(\alpha_0 + \alpha_2 \frac{3m_J^2 - J(J+1)}{J(2J-1)} \right) E_z^2 = -\frac{1}{2} \alpha E_z^2. \quad (2.6)$$

Here J is the quantum number of the total angular momentum and m_J is the corresponding magnetic quantum number. The polarizability α contains a scalar part α_0 and a tensor contribution α_2 which vanishes in the case of $J = 1/2$. Scalar and tensor polarizabilities α_0 and α_2 of selected cesium Rydberg states can be found in Ref. [35]. The action of a rf electric field on atoms is treated in Sec. 7.1.

2.4 Atom-Light Interaction

The interaction between atoms and light can be treated in several different ways each offering distinct advantages [36, 37]. The theoretical framework presented in the following is based on a semiclassical picture in which the atom is treated quantum-mechanically, while the electromagnetic field modes are described as classical plane waves.¹

Framework

The total Hamiltonian of the considered system consists of the atomic Hamiltonian H_a , the Hamiltonian of the electromagnetic field H_l and the Hamiltonian H_{int} which covers the interaction between atom and light field. Since we do not have to consider the photon characteristics of the light field for our purposes, we can safely neglect H_l and the total Hamiltonian reduces to

$$H = H_a + H_{\text{int}}. \quad (2.7)$$

In most cases it is possible to describe the complicated electronic structure of an atom adequately by a much simpler model consisting of only few energy levels which are coupled by near-resonant field modes. A two photon excitation for example might be well described by a three-level model consisting of a ground state and two excited states. Under the assumption that the system of interest can be described by a n -level model, we can write the atomic state of the system as

$$|\Psi(t)\rangle = \sum_{m=1}^n c_m(t) |m\rangle. \quad (2.8)$$

Here $c_m(t)$ determines the contribution of the energy eigenstate $|m\rangle$ to the state of the system at time t . The atomic Hamiltonian then reads

$$H_a = \sum_{m=1}^n \hbar \delta_m |m\rangle \langle m|, \quad (2.9)$$

where $\hbar \delta_m$ is the energy of the state $|m\rangle$. To find an expression for the interaction Hamiltonian H_{int} , we assume that each driven transition $|i\rangle \rightarrow |j\rangle$ in the system is driven by a single near-resonant field mode²

$$\mathbf{E}_{ij} = \frac{1}{2} E_{0,ij} \hat{\epsilon}_{ij} \left(e^{i\omega_{ij}t} + e^{-i\omega_{ij}t} \right). \quad (2.10)$$

¹ This approach is well justified, if the photon characteristics of the light field is negligible.

² Note that the given definition allows for the case that a single mode is resonant to several transitions. It is then labeled differently for each transition.

Here $E_{0,ij}$ is the electric field amplitude of the electromagnetic wave and $\hat{\epsilon}_{ij}$ is a normalized polarization vector. We neglect the spatial dependence of the electromagnetic wave which is well justified if the electromagnetic wavelength is large compared to the size of the atom. In this case, the dipole-approximation is valid and the interaction Hamiltonian is given by $H_{\text{int}} = -\mathbf{d}\mathbf{E}$, where \mathbf{d} is the atomic dipole operator and \mathbf{E} is the total electric field. The interaction Hamiltonian then becomes

$$H_{\text{int}} = \sum_{i \neq j} \frac{\hbar \Omega_{ij}}{2} \left(e^{i\omega_{ij}t} + e^{-i\omega_{ij}t} \right) |i\rangle\langle j|. \quad (2.11)$$

Here the coupling between the levels $|i\rangle$ and $|j\rangle$ is given by the Rabi frequency

$$\Omega_{ij} = -E_{0,ij} \langle i | \mathbf{d} \hat{\epsilon}_{ij} | j \rangle / \hbar \quad (2.12)$$

determined by the electric amplitude of the electromagnetic field and the dipole matrix element of the transition. A detailed description of how to calculate dipole matrix elements using the Wigner–Eckart theorem is given in Sec. 4.3.

If the atomic state is written in terms of a density matrix $\rho = |\psi\rangle\langle\psi|$, the evolution of the considered system is described by the Liouville-von Neumann equation

$$\frac{\partial \rho}{\partial t} = -\frac{i}{\hbar} [H, \rho] + L(\rho). \quad (2.13)$$

The advantage of this master equation approach is that it allows for the incorporation of a decay of the atomic levels described by the Lindblad operator [38]

$$L(\rho) = \sum_m \Gamma_m (c_m \rho c_m^\dagger - \frac{1}{2} c_m^\dagger c_m \rho - \frac{1}{2} \rho c_m^\dagger c_m). \quad (2.14)$$

Here we sum over all decay channels which are characterized by a decay rate Γ_m . For a given decay from $|i\rangle$ to $|j\rangle$, the operator c_m is given by $c_m = |j\rangle\langle i|$.

The rotating frame

To eliminate the fast rotating terms in Eq. 2.13 originating from the time dependence of the electromagnetic field, it is advantageous to transform the system into a rotating reference frame. In order to do so, we define the unitary transformation matrix

$$U = \sum_m e^{-i\eta_m t} |m\rangle\langle m|, \quad (2.15)$$

where we assume that every energy level of the atomic system is reached by a single specific excitation path. η_m is then defined as the sum of the photon frequencies ω_n involved in this excitation path: $\eta_m = \sum_n q_n \omega_n$. Here q_n is +1 for absorbed photons and -1 for emitted photons. Accordingly, η_m is zero for a ground state. With these definitions, the transformed density matrix becomes

$$\tilde{\rho} = U^\dagger \rho U \quad (2.16)$$

and the Hamiltonian transforms to

$$\tilde{H}' = U^\dagger H U - i\hbar U^\dagger \frac{\partial U}{\partial t}. \quad (2.17)$$

While the Hamiltonian H in the laboratory frame contains terms oscillating at the frequencies ω_{ij} and $-\omega_{ij}$ (see Eq. 2.11), \tilde{H}' contains static terms and terms oscillating at $2\omega_{ij}$. Since the dynamics at twice the optical frequency averages to zero on the timescale of observation, we can apply the rotating wave approximation and neglect the rapidly varying terms. The resulting Hamiltonian \tilde{H} is widely used in literature to describe atom-light interaction. The effect of the rotating frame and the rotating wave approximation is illustrated later, when the example of a two-level system is discussed.

The Liouville-von Neumann equation is still valid in the rotating frame, if the Lindblad operator $L(\rho)$ is replaced by $L(\tilde{\rho})$. After solving Eq. 2.13, the populations of the different states are given by the diagonal entries of the density matrix. The coherence between the different levels is given by the off-diagonal elements. As described later, the imaginary part of the coherence determines the absorption of the light mode resonant to the corresponding transition. If the time evolution of the system is not of interest, $\frac{\partial \rho}{\partial t}$ in Eq. 2.13 can be set to zero and the steady state solution can be obtained by solving the emerging system of linear equations. In the following, the specific case of a two-level system is discussed. The four-level system particularly relevant for the described experiment since Rydberg excitation was achieved via two intermediate states, is described in Ch. 4.

Two Level System

To illustrate the effect of the rotating frame, we want to discuss the example of a two-level system which is coupled by a near resonant laser. If we define ground and excited state as $|g\rangle$ and $|e\rangle$ respectively and label the laser frequency ω_{ge} , we can write the Hamiltonian of the system as

$$H = H_a + H_{\text{int}} = \hbar\delta_e|e\rangle\langle e| + \frac{\hbar\Omega_{ge}}{2} \left(e^{i\omega_{ge}t} + e^{-i\omega_{ge}t} \right) (|g\rangle\langle e| + |e\rangle\langle g|) . \quad (2.18)$$

Here the Rabi frequency is assumed to be real, the energy of the ground state is set to zero and the energy of the excited state is $\hbar\delta_e$. A transform of the Hamiltonian into a rotating frame according to Eq. 2.17 yields

$$\tilde{H}' = \hbar(\delta_e - \omega_{eg})|e\rangle\langle e| + \frac{\hbar\Omega_{ge}}{2} \left[\left(1 + e^{-2i\omega_{ge}t} \right) |g\rangle\langle e| + \left(1 + e^{+2i\omega_{ge}t} \right) |e\rangle\langle g| \right] . \quad (2.19)$$

If we drop the terms oscillating with $\pm 2\omega_{ge}$ according to the rotating wave approximation and define the laser detuning as $\Delta_{ge} = \omega_{ge} - \delta_e$, we obtain the time independent Hamiltonian

$$\tilde{H} = -\hbar\Delta_{ge}|e\rangle\langle e| + \frac{\hbar\Omega_{eg}}{2} (|g\rangle\langle e| + |e\rangle\langle g|) . \quad (2.20)$$

Absorption

While on the one hand resonant light fields influence an atomic system, on the other hand the atomic system also influences the light fields. This simple fact can be used in the experiment to probe an ensemble of atoms by means of absorption measurements. For a plane wave of intensity I propagating through a homogeneous medium along the z -direction, the absorption is determined by

$$dI = -\alpha I dz , \quad (2.21)$$

where α is the absorption coefficient. If α does not depend on the intensity I , Eq. 2.21 can be easily integrated to obtain the Beer-Lambert law

$$I(z) = I_0 \exp(-\alpha z). \quad (2.22)$$

The form of the latter expression suggests the definition of an optical density which is a measure for the absorption ability of an atomic ensemble for a specific transition. Commonly the optical density is defined as $OD = \alpha_0 l$, where $\alpha_0 = \alpha(\Delta_{ge} = 0)$ is the resonant absorption coefficient of the considered transition and l is the interaction length of the light field and the atomic ensemble.

Within the presented framework, the absorption coefficient corresponding to a specific transition $|i\rangle \rightarrow |j\rangle$ is proportional to the imaginary part of the coherence $\tilde{\rho}_{ji}$. For a two-level system, α is given by [23]

$$\alpha_{2\text{-level}} = \frac{2n\omega_{ge}}{\varepsilon_0 E_{0,ge} c} d_{ge} \text{Im} \tilde{\rho}_{eg}. \quad (2.23)$$

Here n is the number density of the atomic ensemble, ε_0 is the vacuum permittivity, c is the speed of light and $d_{ge} = \langle g | \mathbf{d} \hat{\mathbf{e}}_{ge} | e \rangle$. Combined with the steady state solution of Eq. 2.13 for a two-level system [23], Eq. 2.23 leads to

$$\alpha_{2\text{-level}} = -\frac{2n\omega_{ge}}{\varepsilon_0 E_{0,ge} c} d_{ge} \frac{\Omega_{ge} \Gamma_{eg}}{2\Omega_{ge}^2 + 4\Delta_{ge}^2 + \Gamma_{eg}^2}. \quad (2.24)$$

If this expression is interpreted as a function of the laser detuning Δ_{ge} , it shows a Lorentzian lineshape with a width of $\Gamma' = \Gamma_{eg} \sqrt{1 + I/I_{\text{sat}}}$, where I is the intensity of the light field and the saturation intensity I_{sat} is defined by $I/I_{\text{sat}} = 2\Omega_{ge}^2/\Gamma_{eg}^2$. For intensities much lower than the saturation intensity, Γ' equals the natural linewidth Γ_{eg} of the transition and α is independent of the intensity. For higher intensities however, power broadening takes place and the linewidth increases. In this case, α is not intensity independent anymore and the Beer-Lambert law is not applicable.

Thermal Atoms

Due to the Doppler effect, the thermal motion in an atomic ensemble leads to a frequency shift of electromagnetic waves in the reference frame of the moving atoms. For a plane wave with angular frequency ω and wave vector \mathbf{k} , this frequency shift is given by

$$\omega' = \omega - \mathbf{k} \mathbf{v}, \quad (2.25)$$

where \mathbf{v} is the atomic velocity. For a spectroscopy setup in which all excitation beams are parallel to each other, only the velocity component of the atoms in beam direction is relevant. If the z -direction is defined accordingly, the relevant velocity distribution of the atoms is thus given by a one-dimensional Maxwell-Boltzmann distribution [39]

$$n(v_z) dv_z = n_0 \sqrt{\frac{m}{2\pi k_B T}} \exp\left(-\frac{mv_z^2}{2k_B T}\right) dv_z. \quad (2.26)$$

Here k_B is the Boltzmann constant, T is the temperature, m is the mass of a single atom and n_0 is the number density of the atomic ensemble. As a consequence of the Doppler effect, the

absorption coefficient of a thermal atomic ensemble is given by the convolution of its velocity distribution and the absorption coefficient of atoms at rest. This leads to

$$\alpha_{\text{therm}} = \int_{-\infty}^{\infty} \alpha(\Delta - kv_z) \sqrt{\frac{m}{2\pi k_B T}} \exp\left(-\frac{mv_z^2}{2k_B T}\right) dv_z, \quad (2.27)$$

where Δ denotes the detuning of the excitation light with respect to the considered transition.

Transit Time Effects

As a consequence of the thermal movement, a single atom only interacts for a limited amount of time with the excitation light of a given spectroscopy setup. This interaction time is determined by the flight time of the atom through the beam. In a theoretical model, the limited interaction time can be accounted for by introducing an effective decay Γ_{tt} . While this is a phenomenological approach, the consequences of a decay are similar to the situation that an atom leaves the interaction region and another ground state atom enters. An expression for the transit time decay given in Ref. [40] is

$$\Gamma_{\text{tt}} = \sqrt{\frac{2}{\ln 2}} \sqrt{\frac{8k_B T}{\pi m}} \frac{1}{d}, \quad (2.28)$$

where d is the $1/e^2$ -beam diameter of the excitation beam and m is the atomic mass.

2.5 Hollow-Core Optical Fibers

Conventional optical fibers, nowadays widely used in telecommunication, consist of a solid core surrounded by a cladding layer. The light-guiding mechanism of these fibers is based on total internal reflection on the core-cladding interface and therefore requires the cladding to have a lower refractive index than the core. For hollow-core fibers without adequate filling, this guiding mechanism breaks down since no cladding material with a refractive index $n < 1$ is available. However, light is guided in hollow-core glass capillaries due to reflection at grazing incidence if the wavelength of the light λ is much smaller than the inner radius of the capillary [41].

In general, three different types of core modes are allowed in a cylindrical geometry such as a capillary. These are transverse circular electric modes (TE), transverse circular magnetic modes (TM) and hybrid modes (EH) [41, 42]. An illustration of the electric field distribution of low order TE, TM and EH modes is shown in Fig. 2.1. For TE and TM modes, only specific electric and magnetic field components are present. For example, the only electric field component of the allowed circular TE modes is E_φ , where φ is the azimuthal angle of the cylindrical coordinate system defined by the geometry of the capillary. For the hybrid modes, all electric and magnetic field components can occur.

If the in-coupled beam into the capillary is Gaussian, only a specific class of hybrid modes labeled EH_{1m} (or HE_{1m}) can be excited [43]. The radial electric field profile of the lowest-loss mode EH_{11} of this class can be approximated by [43]

$$E(r) = E_0 J_0 \left(u_{11} \frac{r}{a} \right), \quad (2.29)$$

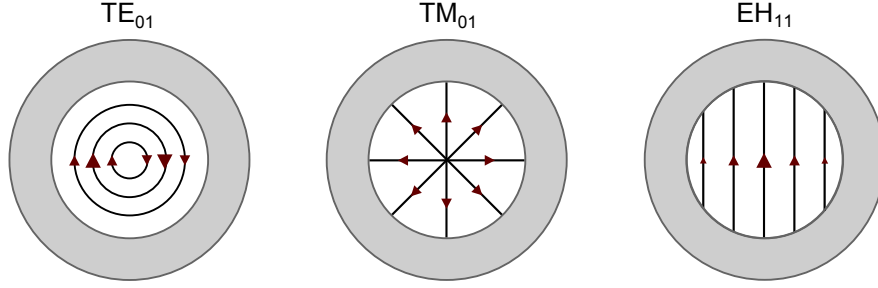


Figure 2.1: Electric field distribution of different light modes in a capillary. Shown are low-order transverse circular electric modes (TE), transverse circular magnetic modes (TM) and hybrid modes (EH). For a Gaussian input beam, the EH_{11} mode represents the lowest-loss mode inside a capillary. The length of the drawn arrows corresponds qualitatively to the field intensity. The drawing is based on a similar illustration given in Ref. [41].

where a is the core diameter of the capillary, J_0 is the zero-order Bessel function of the first kind and u_{11} is the first root of the equation $J_0(u_{11}) = 0$. The maximal coupling efficiency of an incident Gaussian mode with beam waist w to the EH_{11} mode is given in Ref. [43] as $\eta = 98.1\%$ for a ratio of $w/a \approx 0.64$.

In the late 1990s, a new class of light guiding hollow-core fibers was introduced, so-called hollow-core photonic crystal fibers [44]. In contrast to capillaries, the guiding mechanisms of these fibers rely on a periodic structure of the cladding surrounding the hollow core. A specific class of photonic crystal fibers are bandgap fibers which possess a cladding consisting of a periodic lattice of air holes separated from each other by thin silica walls. This air-glass structure of the cladding creates a bandgap for a specific wavelength range and light with a wavelength within this bandgap is confined to the hollow core. A SEM image of the cross section of such a bandgap fiber which was employed in the described experiment (see Sec. 6.1) is shown in Fig. 2.2b. While bandgap fibers show low attenuation of the propagating light (as small as ~ 1 dB/km [45]), the transmission is restricted to a narrow wavelength range corresponding to the bandgap. In contrast, kagome-type hollow-core photonic crystal fibers show a much broader transmission at the cost of a higher propagation loss. The kagome-structured air-glass cladding of these fibers does not create a bandgap. Instead, the guiding mechanism is based on the suppressed coupling of the core modes to the cladding modes [45]. A SEM image of a $60\text{ }\mu\text{m}$ core kagome-type fiber used in the experiment is shown in Fig. 2.2a.

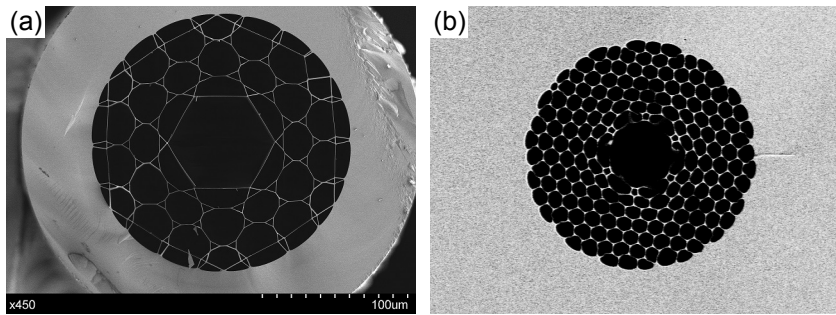


Figure 2.2: SEM images (provided by the Max Planck Institute for the Science of Light – Russell division, Erlangen) of hollow-core photonic crystal fibers. Shown is a $60\text{ }\mu\text{m}$ core kagome-type fiber (a) and a $12\text{ }\mu\text{m}$ core bandgap fiber (b).

While numerical methods are needed to model light guidance in kagome-type fibers [46], the supported modes of both kagome fibers and bandgap fibers are very similar to the modes of a capillary [45]. The fundamental mode of these fibers is therefore HE_{11} -like and shows a similar field distribution as illustrated in Fig. 2.1.

3 Experimental Apparatus

The experiment described in this thesis was built to investigate Rydberg atoms in hollow-core fibers and is the successor of previous work [23, 47, 48]. The new setup features two separate experiment chambers. While the one chamber (in the following referred to as CF-40 chamber) contains a variety of different fibers, the second chamber (in the following referred to as e-chamber) allows to apply individual ac electric fields to different segments along a fiber. The optical setup consists of three laser systems and a spectroscopy setup. The laser systems were already in place at the beginning of this work and are detailed in Ref. [23]. In the following, all components set up in the scope of this thesis are described in more detail.

3.1 Vacuum System

The vacuum system of the experiment is shown in Fig. 3.1. It consists of the two experiment chambers and a pre-chamber. The three chambers are separated from each other with two CF40 all-metal valves, which renders the experiment chambers independent from each other. Due to the common pre-chamber however, the design allows for a single turbo pump (Pfeiffer HiPace 80) and a single gauge (Pfeiffer PKR 261). The turbo pump is backed up by a diaphragm pump (Pfeiffer MVP 040-2). A benchmark for the vacuum pressure required in a system later used for the spectroscopy of cesium vapor, is the vapor pressure of cesium. At room temperature, this corresponds to a pressure on the order of 10^{-6} mbar [31]. The described vacuum system proved to reach pressures on the order of 10^{-8} mbar before it was exposed to cesium and is therefore well suited for its purpose. The two experiment chambers are described in more detail in the following sections.

3.2 CF40-Chamber

To allow for the investigation of Rydberg excitations in different fiber types and various core diameters, the first experiment chamber is equipped with twelve different hollow-core fibers with core diameters ranging from $4\mu\text{m}$ to $62\mu\text{m}$. The fibers are mounted on a 85 mm long stainless steel holder (manufactured in-house from the faculty mechanical workshop) which lies in a CF40 vacuum cube. A photo of both the chamber and the fiber holder is shown in Fig. 3.2 which also contains a list of the installed fibers in the caption. Both ends of the fibers are optically accessible through standard glass viewports. Special care was taken during the design to minimize the distance between the fiber ends and the vacuum windows. To prevent the fibers from moving, they lie in V-grooves and are held in place by small polished copper plates fixed to the holder. One flange of the chamber is connected through a valve to the pre-chamber which in turn is connected to a turbo pump. The opposite flange connects the chamber through a CF16 valve to a flexible metal bellow which can be heated independently from the rest of the chamber and acts as cesium reservoir.

During the assembly of the chamber, a small glass ampule containing cesium was deposited in the reservoir bellow. The chamber was then baked out at 140 °C and pumped to a pressure of 1.7×10^{-8} mbar, before it was cooled down again and the valve to the pre-chamber was closed. Subsequently, the cesium ampule inside the bellow was broken to expose the fibers to a cesium atmosphere.

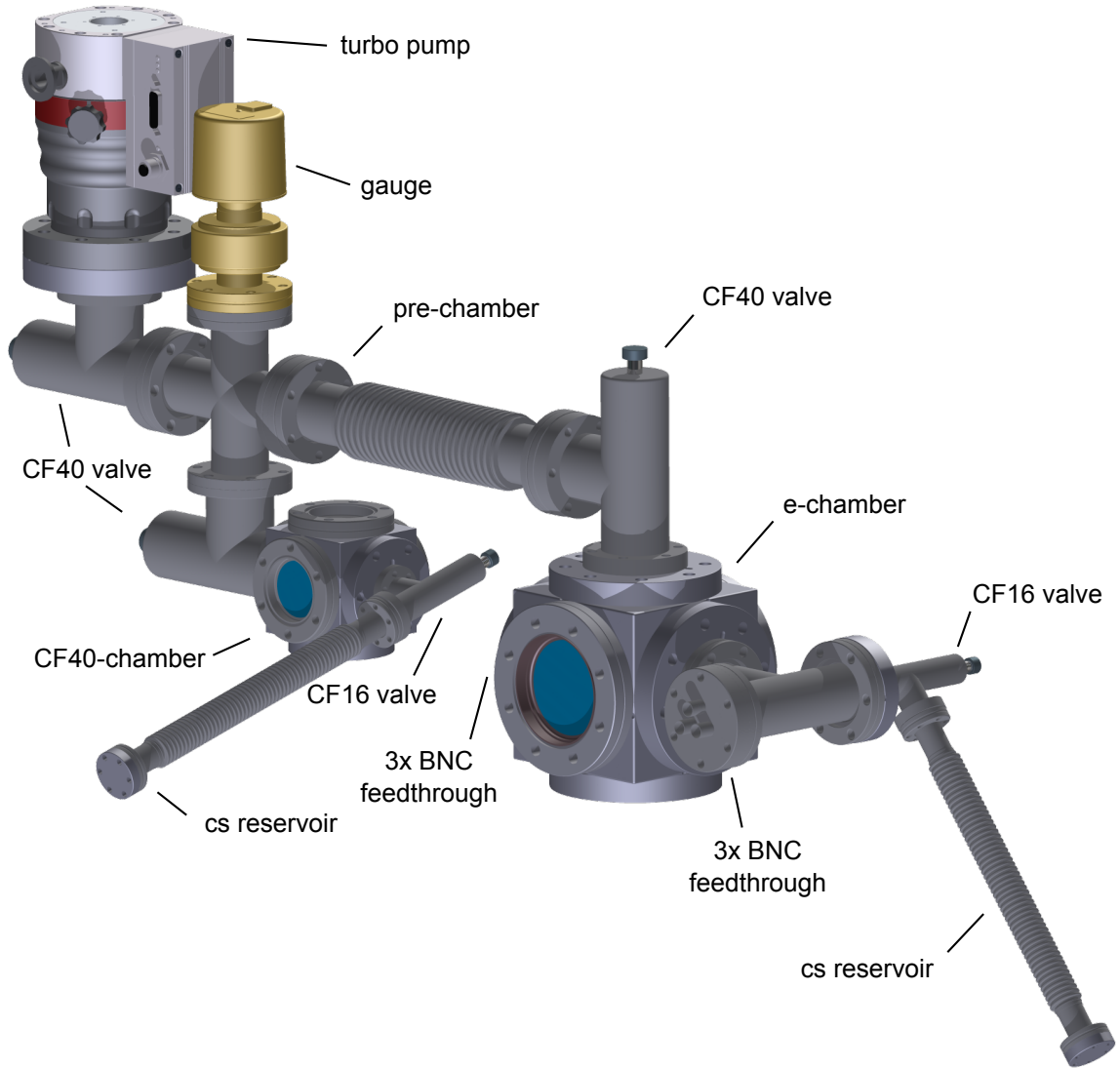


Figure 3.1: CAD sketch of the vacuum system of the experiment. The two experiment chambers, referred to as CF40-chamber and e-chamber share a common pre-chamber and a turbo pump. Only all-metal valves are used in order to ensure the compatibility of all components with cesium. The drawing contains CAD files kindly provided by Kurt J. Lesker Company Ltd., Pfeiffer Vacuum GmbH and VACOM Vakuum Komponenten & Messtechnik GmbH.

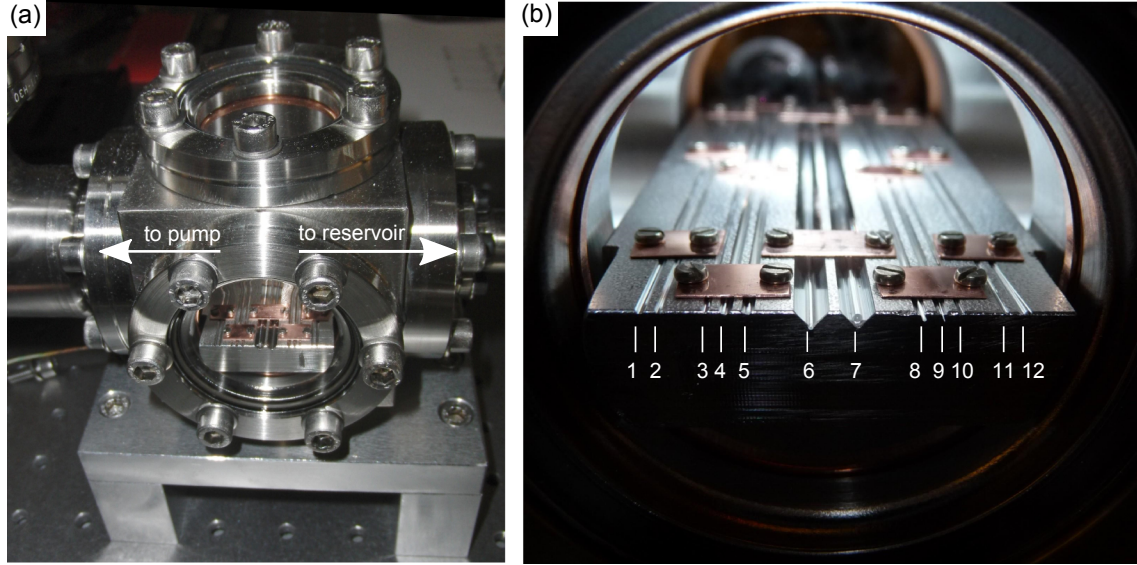


Figure 3.2: (a) CF40-chamber with stainless steel fiber holder inside. The left flange is connected through a valve and a pre-chamber to a turbo pump. The right flange is connected to a cesium reservoir which can be heated independently from the chamber. (b) Fiber holder with different fiber types and core diameters (respectively wall distances for kagome-type fibers): (1) mercedes-type solid core fiber, (2) 27 μm kagome, (3) 12.5 μm kagome, (4) 19.7 μm kagome, (5) 61.6 μm kagome, (6) 20 μm capillary, (7) 60 μm capillary, (8) 36 μm kagome, (9) 43 μm capillary, (10) 6.5 μm capillary, (11) 4.2 μm capillary, (12) 12 μm hollow-core photonic bandgap fiber. All fibers except of (6) and (7) were provided by the Max Planck Institute for the Science of Light (Russell division), Erlangen. Fibers (6) and (7) were provided by MicroQuartz GmbH and IFSW-Institut für Strahlwerkzeuge (Stuttgart), respectively. SEM images of fiber (5) and (12) are shown in Fig. 2.2.

3.3 E-Chamber

The e-chamber (see Sec. 3.1) was designed with the aim of addressing individual segments along a hollow-core fiber by electric fields. To enable the application of ac electric fields (see Ch. 7), an important design consideration was a bandwidth of the field modulation in the upper MHz regime (>100 MHz). The apparatus consists of five individual field plates along the fiber which can be modulated with a frequency of over 2 GHz. This versatile setup does not only allow an individual tuning of the Rydberg resonance, providing a spatial resolution along the fiber, but also allows the study of rf-dressed Rydberg states (see Sec. 7.3). While the spatial resolution along the fiber enables a detailed study of diffusion processes, the latter point is interesting because the setup allows to test the feasibility of miniaturized vapor-based fiber modulators.

In addition to the modulation bandwidth, a major requirement on the apparatus was the cesium compatibility of all parts. While some literature is existent on this topic [49, 50], the knowledge gained from previous experiments of our research group were most beneficial [51, 52]. A detailed description of the relevant components of the device is given in the following. All machined copper parts were manufactured in-house from the faculty mechanical workshop.

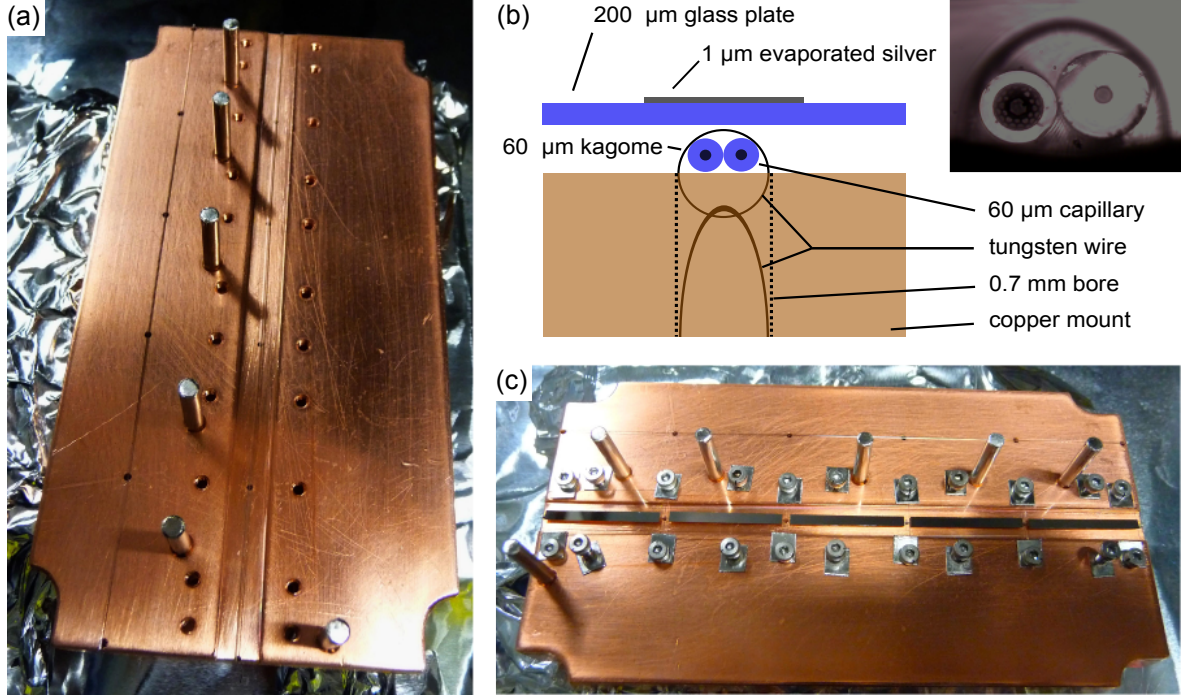


Figure 3.3: Fiber holder which allows for the electrical addressing of five individual fiber segments. (a) A 60 μm core kagome fiber and a 60 μm core capillary are mounted directly next to each other in the central groove of the holder. A 11 μm core capillary is mounted on the left side of the holder (not electrically addressable). Stainless steel pins provide a fastening option for coaxial cables. (b) A loop of thin tungsten wire is fixed to a thicker V-shaped tungsten wire clamped into a 0.7 mm bore and holds the fibers in place. (c) The five field plates (evaporated silver stripes on glass substrates) are mounted above the recessed fibers.

◇ **Chamber.** The e-chamber consists of a stainless steel CF63 cube with an edge length of 114 mm. The upper flange of the cube is connected via a valve to the pre-chamber which in turn is connected to the turbo pump (see Sec. 3.1). Two opposite viewports allow for optical access. The other two flanges on the side of the cube lead to two electrical feedthroughs (each offering three BNC connections on the air-side) and the cesium reservoir in form a metallic bellow. Both the chamber and the reservoir can be heated independently. As for the CF40-chamber, a glass ampule containing cesium was deposited in the reservoir bellow and broken from the outside after the baking process.

◇ **Fiber holder.** The fiber holder illustrated in detail in Fig. 3.3 is made of a 10 mm copper plate which lies in the circular openings of the vacuum cube (see Fig. 3.4). Accounting for additional space in the viewports, the length of the holder is 116 mm, which is also the length of all mounted fibers. In total, three fibers are mounted on the holder: a 11 μm core capillary, a 60 μm core kagome fiber (see Fig. 2.2a) and a 60 μm core capillary.¹ While the 11 μm capillary (which is not electrically addressable) is mounted at the side of the holder, the other two fibers are mounted in a central groove of 6 mm \times 0.4 mm. The fibers are fixed to the holder in 23 mm intervals using small loops of 42 μm tungsten wire which are held in place by V-shaped 170 μm tungsten wires clamped into 0.7 mm bores (see Fig. 3.3b).

¹ Both capillaries were provided by MicroQuartz GmbH, München. The kagome fiber was provided by the Max Planck Institute for the Science of Light (Russell division), Erlangen.

M2 threads on either side of the central groove provide a mounting option for the field plates positioned above the fibers. 2.9 mm stainless steel pins screwed to the holder act as holder for coaxial cables connecting the field plates to the feedthroughs. Since the coaxial cables, the chamber and the fiber holder are on common ground, copper was chosen for its high conductivity to minimize standing wave effects. It should be noted, that no oxygen-free copper was used and the standard copper proved to be compatible with the demands on the vacuum required for Rydberg spectroscopy in thermal cesium vapor. To avoid hollow spaces in the mount which could cause virtual leaks in the vacuum chamber, all holes are through-holes and only vented screws have been used.

- ◇ **Field plates.** The five field plates consist of evaporated silver stripes with a width of 2 mm on glass substrates of $22.5 \text{ mm} \times 9 \text{ mm} \times 0.2 \text{ mm}$.¹ To ensure a good bond between the glass and the silver, an approximately 5 nm thick layer of chromium has been deposited between the glass and the approximately 1 μm thick silver layer. The glass plates which have a larger width than the central groove of the fiber holder are mounted with the silver stripes centered over the fibers and facing up (see Fig. 3.3c). The fastening of the glass plates with thin stainless steel brackets ensures that no excessive forces caused by thermal expansion can destroy the field plates.

A main consideration while designing the field plates was to minimize the capacity formed by the plate and the fiber holder to ensure a high modulation bandwidth. The capacity of a single field plate above the fiber holder is on the order of 1 pF. For frequencies in the MHz regime, such a small capacitance essentially constitutes an open end. The voltage between the field plate and the fiber holder which is connected to ground, can therefore

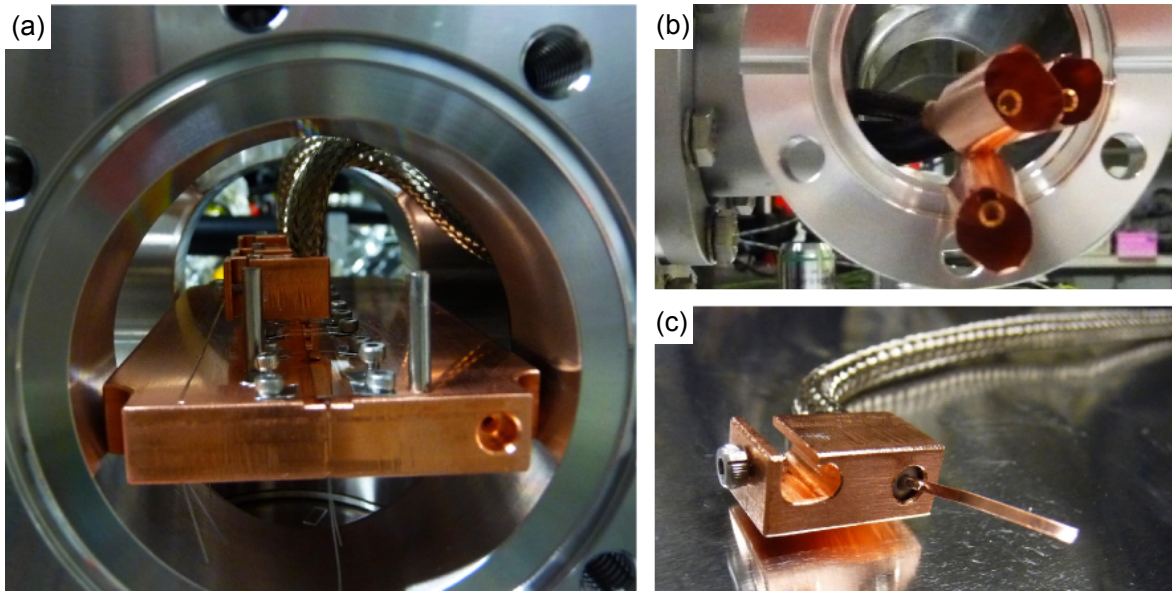


Figure 3.4: (a) Assembly of the self-built coaxial cables for three of the five cables installed on the fiber holder. (b) Beryllium-copper contacts are used as a connection to the feedthroughs. To ensure a continuous shielding of the cable, thin tubes of copper foil surround the contacts. (c) Coaxial cable with copper mount which is used to install the cable to the fiber holder. The contact between the central conductor and the field plates is ensured by thin copper stripes.

¹ The evaporation was kindly performed by the 1st Institute of Physics of our university.

be estimated to be twice the applied voltage. Since the length of the silver stripes is small compared to the wavelength of the applied electromagnetic waves, the resistance of the evaporated layer due to the skin effect [53], can be neglected.

- ◇ **Coaxial cables.** To avoid unwanted cross-talk between the individual field plates, the latter are connected through coaxial cables to the feedthroughs. Although vacuum compatible coaxial cables are commercially available, almost all of these are not compatible with high density cesium vapor due to the high reactivity of cesium. As a consequence, the cables were self-built out of alumina beads lined up on a central conductor and surrounded by a conductive braiding. The ends of the cables connected to the field plates are held in copper mounts attached to the stainless steel pins screwed into the fiber holder (see Fig. 3.4c). As central conductor and braiding, 1 mm silver plated copper wire and nickel plated copper braid was used respectively. The residual magnetization of the nickel coating was measured to cause a magnetic field on the order of 100 mG at mm distances from the cable. Considering that this corresponds to a Zeeman shift [54] on the order of kHz for the involved atomic states in the experiment, the influence of the cables on the atomic system can be neglected in the context of this work. Due to the specific size of the alumina beads, the cable has an impedance of approximately $28\ \Omega$. Since the BNC feedthroughs have an impedance of $50\ \Omega$, standing wave effects create a small frequency dependence of the transmission of the cable. Although this effect was observed in the experiment, it did not limit the modulation bandwidth up to 2 GHz which was the maximum frequency of the employed radio-frequency generator (see Sec. 7.2).
- ◇ **Field plate connection.** The central conductors of the coaxial cables are connected to the field plates through $30\ \mu\text{m}$ thick copper stripes crimped to the slit end of the cables (see Fig. 3.4c). The stripes are pressed on the field plates by small $5\ \text{mm} \times 9\ \text{mm} \times 0.2\ \text{mm}$ glass plates held in place by stainless steel brackets (see Fig. 3.3c). The assembly of the coaxial cables is shown in Fig. 3.4a for three of the five cables installed on the fiber holder.
- ◇ **Feedthroughs.** The electrical feedthroughs used offer a BNC connection on the air-side and a 2.39 mm connector pin on the vacuum-side surrounded by a grounded shield. In total, six connections distributed on two feedthroughs are available, five of which are used. The in-vacuum coaxial cables are connected with beryllium-copper contacts to the feedthroughs (see Fig. 3.4b). A continuous shielding of the central conductor is ensured by thin tubes of $30\ \mu\text{m}$ copper foil which surround the beryllium-copper contacts. In contrast to the coaxial cables themselves, the connection between the feedthroughs and the cables does not have a well-defined impedance. However, the corresponding cable segment is short and is expected to have little impact on the transmission characteristics for the modulation frequencies considered here.

3.4 Optical Setup

Rydberg excitation is achieved via a three-photon process involving the wavelengths 895 nm, 1359 nm and 780 nm (see Sec. 4.1). The excitation light is delivered by means of optical fibers to the setup. Following the notation used in Ref. [55], the lasers corresponding to the three excitation wavelengths are in the following referred to as probe laser, dressing laser

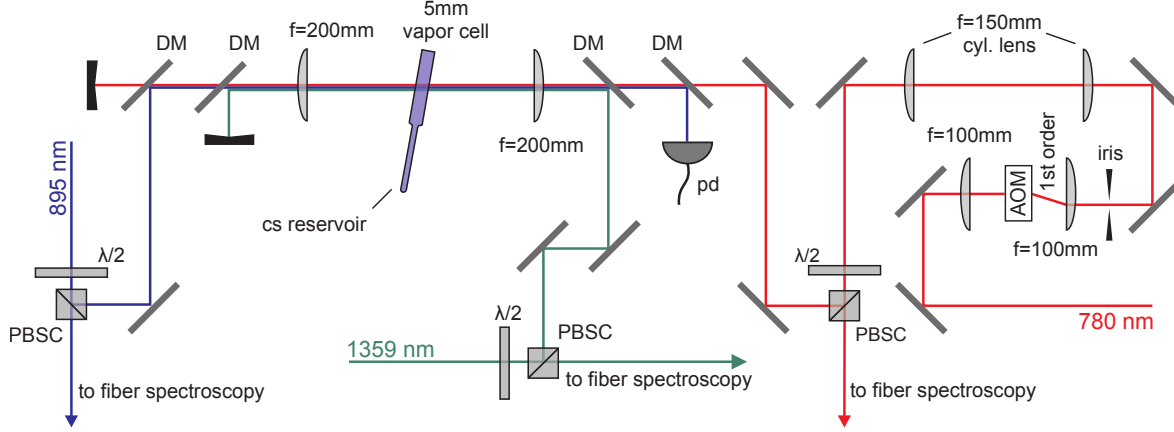


Figure 3.5: Setup of the reference spectroscopy which uses a 5 mm vapor cell. The probe beam (895 nm) which counter-propagates with respect to the dressing (1359 nm) and coupling (780 nm) beams through the cell is detected with a photodiode (pd). Dichroic mirrors (DM) are used to combine and split the three beams. Combinations of half-wave waveplates ($\lambda/2$) and polarizing beam splitter cubes (PBSC) are used to adjust the beam powers. All beams are focused into the cell with $f = 200$ mm lenses. To enable the use of a lock-in amplifier, the coupling beam can be amplitude modulated with an acousto-optic modulator (AOM).

and coupling laser respectively. The setup itself consists mainly of three parts which can be related to the two experiment chambers and a reference spectroscopy setup.

◇ **Reference spectroscopy.** To allow for the investigation of fiber-induced line shifts and broadenings, a reference spectroscopy setup containing a 5 mm vapor cell is included in the experiment (see Fig. 3.5). The cell consists of the actual cell body where the spectroscopy takes place, and an attached reservoir. Cell and reservoir can be heated independently from each other. The atomic number density of the cesium vapor inside the cell can be controlled according to Eq. 2.1 by the reservoir temperature. The 895 nm probe beam is focused into the spectroscopy cell with a 200 mm lens, subsequently collimated with a second 200 mm lens and directed on a photodiode with a dichroic mirror. The 1359 nm dressing beam and the 780 nm coupling beam counter-propagate with respect to the probe beam in order to partly cancel the Doppler-effect. Dichroic mirrors are used to overlap both beams with the probe beam. After passing the spectroscopy cell, they are separated again from the probe beam. The $1/e^2$ -radii of probe, dressing and coupling beam inside the spectroscopy cell are approximately $w_p = 57 \mu\text{m}$, $w_d = 71 \mu\text{m}$ and $w_c = 72 \mu\text{m}$. All beam powers can be adjusted with combinations of half-wave wave plates and polarizing beam splitters. Typical beam powers employed in the experiment are $p_p = 300 \text{ nW}$, $p_d = 10 \mu\text{W}$ and $p_c = 50 \text{ mW}$ for probe, dressing and coupling beam respectively. To enable the use of a lock-in amplifier, the 780 nm beam can be amplitude modulated with an acousto-optic modulator (AOM).

◇ **CF40-chamber.** The spectroscopy setup for the CF40-chamber is shown in Fig. 3.6. The three beams combined in the same way as in the reference spectroscopy, are focused into the fibers with two achromatic lenses or $10\times$ microscope objectives¹ mounted on 3D translation stages. For the $60 \mu\text{m}$ kagome fiber, coupling efficiencies of $\eta_{895} \approx 57 \%$, $\eta_{1359} \approx 60 \%$ and

¹ Nikon TU Plan Fluor $10\times/0.30$ A.

$\eta_{780} \approx 60\%$ were obtained with 40 mm lenses. The fiber ends can be imaged onto two CCD cameras to enable optimization of the mode profile of the three beams inside the fiber. A freespace 895 nm reference beam through the chamber allows for optical density measurements outside of the fibers.

- ◇ **E-chamber.** The optical setup around the e-chamber closely resembles the spectroscopy setup for the CF40-chamber shown in Fig. 3.6. Two 50 mm achromatic lenses on linear translation stages are used to couple the three beams into the hollow-core fibers. For the 60 μm kagome fiber, typical coupling efficiencies of $\eta_{895} \approx 54\%$, $\eta_{1359} \approx 33\%$ and $\eta_{780} \approx 55\%$ were obtained. For the 60 μm capillary, loss during the propagation of the light through the capillary is expected to play a bigger role than for the kagome fiber. The values of $\eta_{895} \approx 23\%$, $\eta_{1359} \approx 6\%$ and $\eta_{780} \approx 32\%$ therefore must be interpreted as in-out efficiencies.

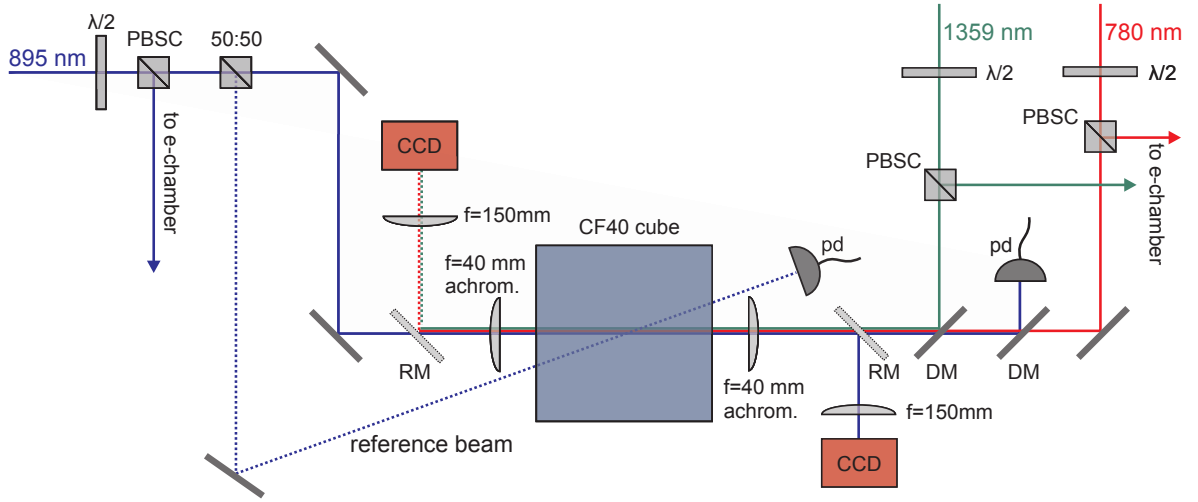


Figure 3.6: Setup of the fiber spectroscopy in the CF40-chamber which closely resembles the reference spectroscopy (see Fig. 3.5). The beams are coupled into the fibers mounted in the vacuum cube by means of two achromatic lenses or two 10 \times microscope objectives. Removable mirrors (RM) are used to image the fiber ends onto CCD cameras in order to optimize the mode profiles. A 895 nm reference beam split from the beam path with a fifty-fifty beam splitter (50:50) is used to monitor the optical density in the chamber. Used abbreviations: DM (dichroic mirror), PBSC (polarizing beam splitter cube, $\lambda/2$ (half-wave waveplate) and pd (photodiode).

4 Three-Photon Rydberg Spectroscopy

In the described experiment, Rydberg excitation in thermal cesium vapor is achieved via a three-photon process involving the intermediate states $6P_{1/2}$ and $7S_{1/2}$. The excitation scheme and the characteristic lineshape of the corresponding spectroscopic signal is discussed in the first part of this chapter. Subsequently, a theoretical model of the atomic system is described and compared to experimental results in the last section of the chapter.

4.1 Excitation Scheme

The excitation scheme $6S_{1/2} \rightarrow 6P_{1/2} \rightarrow 7S_{1/2} \rightarrow nP$, where nP stands for a Rydberg state with total angular momentum $J = 1/2$ or $J = 3/2$ is shown in Fig. 4.1 together with a partial energy level diagram of cesium and the decay rates of the involved states. A major advantage of the system is, that all three excitation steps correspond to near-infrared transition wavelengths for which inexpensive, high-power diode lasers are commercially available. Additionally, all wavelengths correspond to energies below the work function of cesium [58]

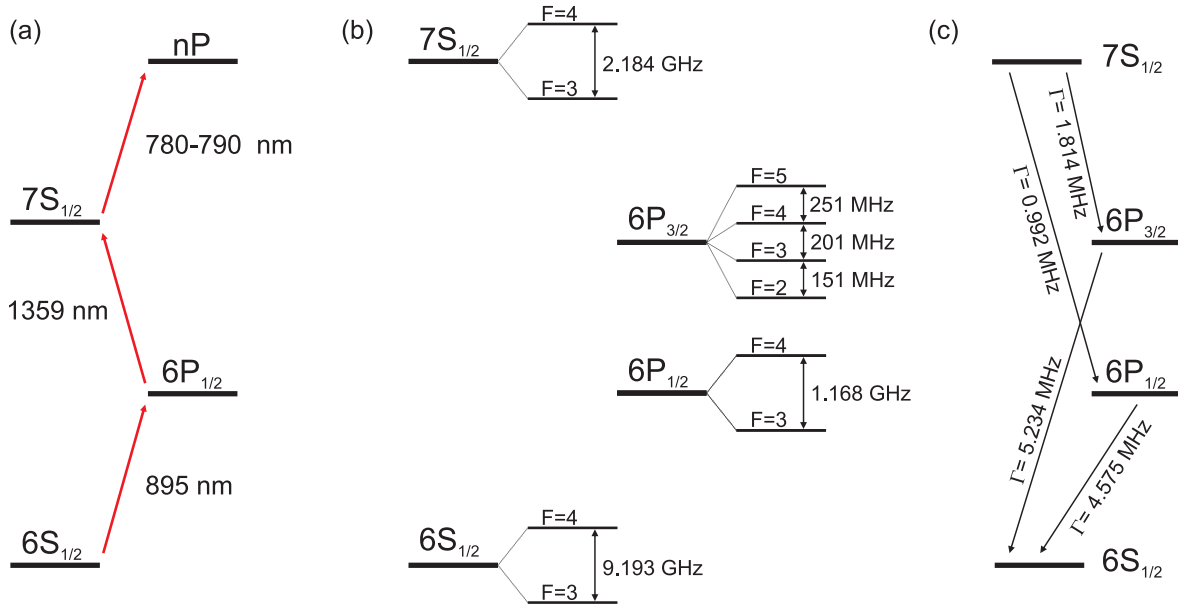


Figure 4.1: (a) Excitation to the Rydberg state is achieved via the two intermediate states $6P_{1/2}$ and $7S_{1/2}$. The first two transitions correspond to transition wavelengths of 895 nm and 1359 nm. The transition wavelength of the last excitation step depends on the main quantum number n of the Rydberg state and ranges from 780 nm to 790 nm for $n = 60$ and $n = 26$ respectively (see Ch. A). (b) Partial energy level diagram of cesium (5D states not included). Energy level spacings [31, 56] rounded to MHz precision. (c) Decay rates of low lying states relevant for the experiment [31, 57]. The lifetime of the Rydberg state is on the order of several μ s and its decay therefore dominated by transit time effects in the experiment (see Sec. 2.4).

which presumably prevents the photo-ionization of cesium deposited on the glass windows of the vacuum chamber and the fiber walls [25].

The first transition which corresponds to the D_1 line is driven with a grating stabilized 895 nm diode laser (Toptica DL 100 pro). During the measurements, the laser was frequency-stabilized to the transition $|6S_{1/2}, F = 3\rangle \rightarrow |6P_{1/2}, F' = 4\rangle$ by means of Doppler-free saturation spectroscopy in a magnetic field [59]. The second transition is driven by a grating stabilized 1359 nm diode laser (Toptica DL 100 pro) which is frequency stabilized to the transition $|6P_{1/2}, F' = 4\rangle \rightarrow |7S_{1/2}, F'' = 4\rangle$ via two-photon polarization spectroscopy [60]. The transition wavelength between the $7S_{1/2}$ state and the Rydberg state lies between 780 nm and 790 nm for main quantum numbers between $n = 60$ and $n = 26$ respectively (see Ch. A). While both a $J = 1/2$ and a $J = 3/2$ state exists for the Rydberg P state, mostly the $J = 3/2$ state was excited in the described work due to its greater coupling strength to the $7S_{1/2}$ state. The corresponding transition is driven with the output of a tapered amplifier¹ which is seeded with a tunable, grating stabilized 780 nm diode laser (Toptica DL pro). During the measurements, the laser was scanned across the Rydberg line. As a frequency reference, the transmission signal of a Fabry-Perot interferometer with a free spectral range of 988 MHz was used. In order to avoid temperature induced drifts of the interferometer, it was actively length-stabilized using the transmission signal of the locked 895 nm laser [23].

4.2 Lineshape of the Three-Photon Signal

During measurements, both the probe laser and the dressing laser were frequency stabilized. The coupling laser was scanned across the Rydberg line and the transmission of the probe laser was monitored with a photodiode. In order to partly cancel the Doppler-effect, all spectroscopy setups were built in such a way that the probe beam counter-propagates with respect to the other two beams (see Sec. 3.4).

For a deeper understanding of the considered atomic system, it is helpful to change from the bare atomic state picture to a semi-dressed state picture in which the two intermediate states are replaced by the new eigenstates originating from the action of the dressing laser on the atomic system [55]. If the dressing laser is resonant with respect to the intermediate transition, the resulting dressed states $|d^+\rangle$ and $|d^-\rangle$ exhibit an energy splitting of Ω_d/\hbar , where Ω_d is the Rabi frequency of the dressing laser (see Fig. 4.2a). The resulting level scheme can be interpreted as two three-level ladder-type systems with intermediate states $|d^+\rangle$ and $|d^-\rangle$ respectively. Due to the action of the dressing laser, the probe laser is off-resonant to the dressed states $|d^\pm\rangle$. For thermal atoms however, the frequency of the probe light is shifted in the rest-frame of the moving atoms due to the Doppler effect (see Sec. 2.4). As a consequence, the probe laser drives the transition $6S_{1/2} \rightarrow |d^\pm\rangle$ for two distinct velocity classes v^\pm .

In the considered atomic system, the absorption of the probe laser is determined by the imaginary part of the coherence between ground state and first excited state $\text{Im}(\rho_{21})$ (see Sec. 4.3) and is therefore accessible in simulations based on a density matrix approach. Fig. 4.2b shows $\text{Im}(\rho_{21})$ obtained from the simulation of a four-level system (representing the states $6S_{1/2}, 6P_{1/2}, 7S_{1/2}$ and the Rydberg state) based on the semiclassical approach

¹ Eagleyard EYP-TPA-0780-01000-3006-CMT03-000.

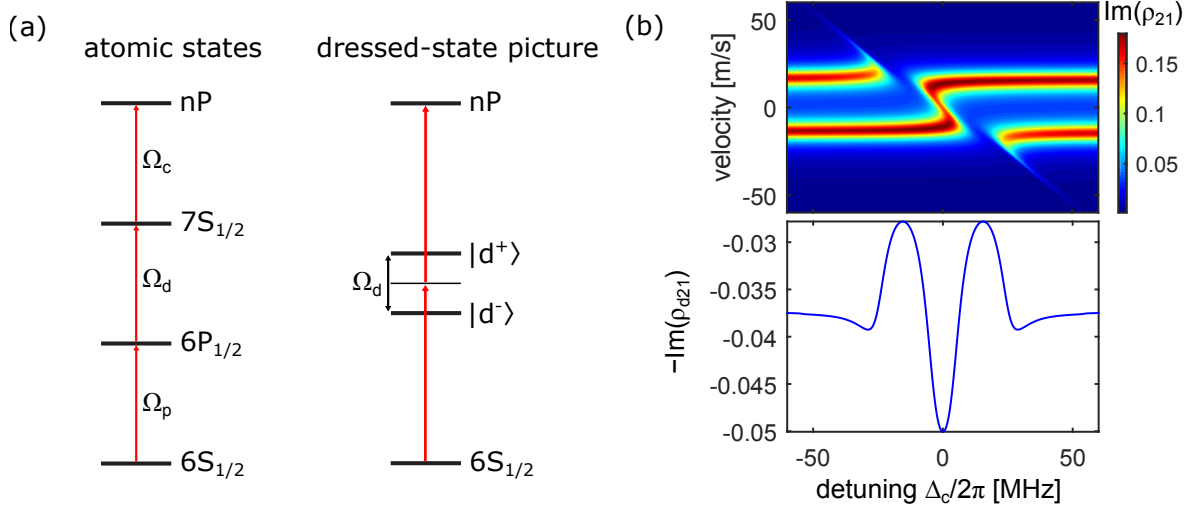


Figure 4.2: (a) Left: Bare atomic states coupled by Rabi frequencies Ω_p , Ω_d and Ω_c . Right: Semi-dressed state picture including the eigenstates $|d^\pm\rangle$ originating from the action of the dressing laser on the system. The image is based on a similar illustration in Ref. [55]. (b) Four level simulation of the considered system for $\lambda_d = 790$ nm, $\Omega_p = 2\pi \times 5$ MHz, $\Omega_d = 2\pi \times 20$ MHz, $\Omega_c = 2\pi \times 10$ MHz, $\Gamma_{21} = 2\pi \times 4.6$ MHz, $\Gamma_{31} = 2\pi \times 1.8$ MHz, $\Gamma_{32} = 2\pi \times 1$ MHz, $\Gamma_{41} = 2\pi \times 1$ MHz. Top: Dependence of $\text{Im}(\rho_{21})$ (which determines the absorption of the probe laser) on the coupling laser detuning Δ_c for different velocity classes. Bottom: Doppler-average of $\text{Im}(\rho_{21})$.

introduced in Sec. 2.4. Since the absorption of the probe laser depends both on the detuning of the coupling laser Δ_c and the one-dimensional velocity of the thermal atoms along the laser axis, the result is shown in form of a velocity-detuning map (top of figure). For an atomic ensemble, $\text{Im}(\rho_{21})$ has to be averaged over all relevant velocity classes, weighted by a one-dimensional Boltzmann distribution (see Sec. 2.4). The resulting quantity $\text{Im}(\rho_{d21})$ is shown in the bottom of Fig. 4.2b.

The two distinct velocity classes v^\pm which probe the dressed states $|d^\pm\rangle$ are clearly visible in Fig. 4.2b for large coupling laser detunings Δ_c . As Δ_c approaches zero, two avoided crossings occur which are due to the coupling of the two dressed states $|d^\pm\rangle$ to the Rydberg state [61, 62]. The typical lineshape of the three-photon signal characterized by two off-resonant features of enhanced transmission and an absorptive feature on resonance ($\Delta_c = 0$) is a direct consequence of this double avoided crossing.

If the magnetic substructure of the atom is taken into account (see Sec. 4.3), the features visible in the top panel of Fig. 4.2b wash out due to different coupling strengths of the individual sublevels. However, the qualitative lineshape of the Doppler-averaged signal remains similar to the one obtained from the four-level system.

4.3 Simulations

While the four-level model introduced in the previous section is suited to describe the considered atomic system for a limited range of Rabi frequencies [23], the influence of the magnetic sublevels is neglected. Moreover, the real atomic system possesses a dark state in form of a hyperfine level which is not coupled to any excited state (see Fig. 4.1). In the following, a theoretical model based on the semiclassical theory discussed in Sec. 2.4 is introduced

which accounts for the involved magnetic sublevels and pumping effects into the dark ground state. The results of the theoretical model are compared to experimental data in the following section.

Level Scheme

Fig. 4.3a shows the considered level scheme for the excitation pathway $|6S_{1/2}, F=3\rangle \rightarrow |6P_{1/2}, F'=4\rangle \rightarrow |7S_{1/2}, F''=4\rangle \rightarrow |nP_{3/2}\rangle$ (excluding the dark ground state). For each of the lower three involved states, two hyperfine states exist. For the Rabi frequencies relevant in the described experiment, only one of these two states is coherently coupled to the rest of the system by lasers (see Fig. 4.1). The whole manifold of these coupled hyperfine states is included in the model. Since the system is coupled via incoherent decay processes to the $|6S_{1/2}, F=4\rangle$ state, a dark state is included in the description. This state represents all sublevels of the $F=4$ state and allows an adequate modeling of pumping processes.

The considered Rydberg state $nP_{3/2}$ possesses four nearly degenerate hyperfine levels which can not be resolved in the experiment. An adequate description can therefore be given in terms of the total angular momentum quantum numbers J and m_J . To simplify the theoretical treatment, it is however advantageous to stay in the F, m_F basis. Due to the selection rule $\Delta F = 0, \pm 1$, three of the hyperfine levels ($F=3, 4, 5$) are coupled to the $7S$ state. Since all three of these states can be regarded as degenerate, they can be represented by a single state for each quantum number m_F [62] which couples to the $7S$ state with an effective Rabi frequency Ω_{eff} . The coupling strength of the involved levels is discussed in the following.

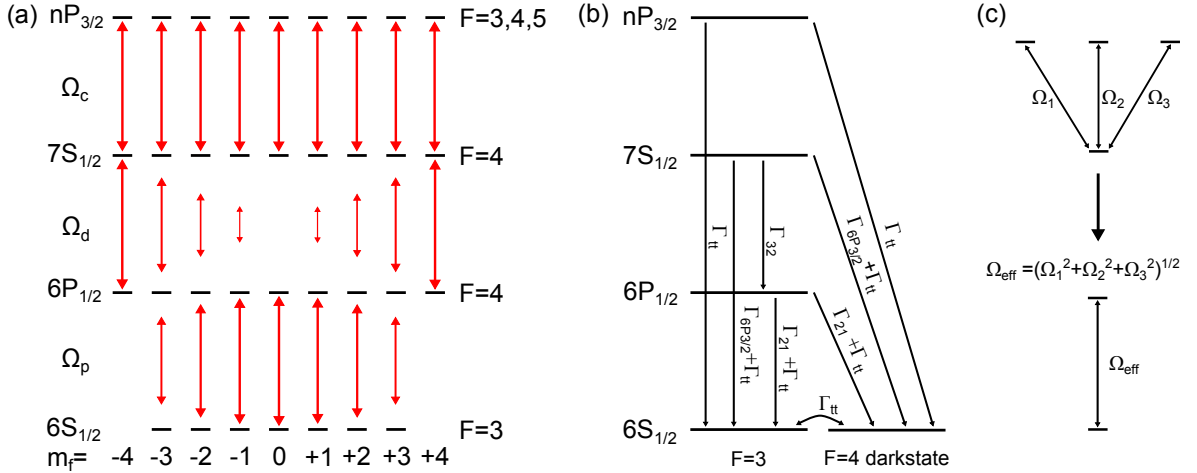


Figure 4.3: (a) Considered level scheme in the theoretical model. In addition to the shown levels, also the dark ground state $|6S_{1/2}, F=4\rangle$ is included. The length of the drawn arrows represents the relative coupling strengths of the levels for linearly, parallel polarized excitation beams. (b) Considered decays in the system. In addition to the natural decays, also a transit time decay Γ_{tt} is included in the model. (c) The hyperfine levels of the Rydberg state are nearly degenerate and are represented by a single state for each quantum number m_F . This can be justified by diagonalizing the Hamiltonian of the shown four-level system in which the coupling of the lower state to the excited states can be expressed in terms of an effective Rabi frequency $\Omega_{\text{eff}} = \sqrt{\Omega_1^2 + \Omega_2^2 + \Omega_3^2}$.

Couplings

From the Hamiltonian discussed in Sec. 2.4 it can be seen that the laser induced coupling between two individual levels of a n -level system is given by the corresponding Rabi frequency Ω . For a transition from state $|i\rangle$ with quantum numbers F and m_F to state $|j\rangle$ with quantum numbers F' and m'_F , the Rabi frequency can be defined as

$$\Omega_{ij} = -\frac{E}{\hbar} \langle F, m_F | \mathbf{d} \hat{\varepsilon} | F', m'_F \rangle, \quad (4.1)$$

where E and $\hat{\varepsilon}$ denote the amplitude and the polarization vector of the coupling field respectively. The dipole operator $\mathbf{d} = e\mathbf{r}$ is given by the elementary charge e and the position operator \mathbf{r} . For a given polarization, the product $\mathbf{d} \hat{\varepsilon}$ can be expressed in terms of the components r_q of \mathbf{r} in the spherical basis. This yields $\mathbf{d} \hat{\varepsilon} = er_q \equiv d_q$, where $q = 0, \pm 1$ for π and σ^\mp polarization respectively. Using this notation and the Wigner-Eckart theorem, the matrix element contained in Ω_{ij} can be factored into an angular part containing a Wigner 3- j symbol and an angular independent, reduced dipole matrix element $\langle F || e\mathbf{r} || F' \rangle$ [31]:

$$\langle F, m_F | d_q | F', m'_F \rangle = \langle F || e\mathbf{r} || F' \rangle (-1)^{F'-1+m_F} \sqrt{2F+1} \begin{pmatrix} F' & 1 & F \\ m'_F & q & -m_F \end{pmatrix}. \quad (4.2)$$

Since transition dipole matrix elements are commonly given in terms of reduced matrix elements in the J basis, it is useful to further reduce this expression by employing the relation [31]

$$\langle F || e\mathbf{r} || F' \rangle = \langle J || e\mathbf{r} || J' \rangle (-1)^{F'+J+1+I} \sqrt{(2F'+1)(2J+1)} \begin{Bmatrix} J & J' & 1 \\ F' & F & I \end{Bmatrix}, \quad (4.3)$$

which contains a Wigner 6- j symbol and the nuclear spin quantum number I . The reduced matrix elements $\langle J || e\mathbf{r} || J' \rangle$ relevant for this work are given in Ch. A. Since all beams are polarized linearly and parallel to each other in the experiment, it is useful to define the quantization axis of the problem in such a way, that $q = 0$. In this case, only transitions with $\Delta m = 0$ are allowed.

For the Rydberg transition, the treatment described above is not suitable since the three hyperfine levels which are coupled to the $7S$ state are represented by a single state for each quantum number m_F . This can be justified by considering a four-level system in which a single state is coupled to three degenerate states, as illustrated in Fig. 4.3c. If the Rabi frequencies are Ω_1 , Ω_2 and Ω_3 , it can be shown by diagonalizing the corresponding Hamiltonian that the coupling of the lower state to the excited states is adequately described by an effective Rabi frequency

$$\Omega_{\text{eff}} = \sqrt{\Omega_1^2 + \Omega_2^2 + \Omega_3^2}. \quad (4.4)$$

A similar approach was used in Ref. [62] to reduce a Y -type three-level system to a two-level system. Using Eq. 4.4, the Rabi frequency for the transition $|7S_{1/2}, F=4, m_F\rangle \rightarrow |nP_{3/2}, m_F\rangle$ can be given as

$$|\Omega_{\text{eff}}| = \frac{E}{\hbar} \sqrt{\sum_{F'=3,4,5} |\langle F=4, m_F | d_0 | F', m_F \rangle|^2}. \quad (4.5)$$

The coupling strengths of the individual levels determined with the theoretical frame work described above is illustrated in Fig. 4.3a. For the sake of clarity, it is desirable to characterize

the system by only three coupling strengths. Throughout the rest of this thesis, coupling and dressing Rabi-frequencies Ω_p and Ω_d are therefore given in terms of the definition

$$\Omega_{p,d} = -\frac{E}{\hbar} \langle F \| e\mathbf{r} \| F' \rangle \quad (4.6)$$

and have to be interpreted accordingly. In the case of the Rydberg transition, the definition

$$\Omega_c = -\frac{E}{\hbar} \langle J \| e\mathbf{r} \| J' \rangle \quad (4.7)$$

is used. The electric field amplitude E appearing in both definitions can be determined in the experiment by translating the measured beam power p into an intensity I and using the relation $I = 1/2c\varepsilon_0 E^2$. Here c is the speed of light and ε_0 is the vacuum permittivity. The resulting electric field amplitude is given by

$$E = \sqrt{\frac{2p}{\pi\varepsilon_0 cr^2}}, \quad (4.8)$$

where r is the $1/e^2$ radius of a Gaussian laser beam.

Decays

While the linearly polarized lasers only couple states with $\Delta m = 0$, decay processes mix states with different magnetic quantum numbers, since $\Delta m = 0, \pm 1$ in this case. The decay rate of all magnetic sublevels of an excited state with quantum number J' into a lower state with quantum number J , is equal and given by [31]

$$\Gamma = \frac{\omega_0^3}{3\pi\varepsilon_0\hbar c^3} \frac{2J+1}{2J'+1} |\langle J \| e\mathbf{r} \| J' \rangle|^2, \quad (4.9)$$

where ω_0 is the resonance frequency of the transition. This total decay rate, given in Fig. 4.1 for the relevant transitions, represents the sum of the decays into the individual sublevels of the lower state. The decay into a specific sublevel of the lower state can be found using the relation [31]

$$\sum_{q,F} |\langle F, m'_F + q | d_q | F', m'_F \rangle|^2 = \frac{2J+1}{2J'+1} |\langle J \| e\mathbf{r} \| J' \rangle|^2, \quad (4.10)$$

where the sum is taken over the lower state hyperfine levels and $q = 0, \pm 1$. The combination of the last two equations reveals that the excited state $|J', F', m'_F\rangle$ decays into the state $|J, F, m_F = m'_F + q\rangle$ with the decay rate

$$\Gamma_{q,F} = (2F+1)(2F'+1)(2J'+1) \left| \begin{pmatrix} F' & 1 & F \\ m'_F & q & -(m'_F + q) \end{pmatrix} \right|^2 \left| \begin{Bmatrix} J & J' & 1 \\ F' & F & I \end{Bmatrix} \right|^2 \Gamma. \quad (4.11)$$

For an appropriate description of the experimental situation, not only the natural decays, but also transit time effects have to be taken into account (see Sec. 2.4). The limited interaction time of the atoms with the laser light can be treated as an isotropic decay of all states into the sublevels of the two hyperfine ground states. This includes an effective decay between the ground state sublevels themselves. The natural decay of the Rydberg state is on the order of kHz and the transit time decay Γ_{tt} given by Eq. 2.28 is larger than $2\pi \times 0.5$ MHz

for all relevant beam sizes in the considered experiment. As a consequence, all natural decay channels of the Rydberg state are neglected in the model and only a transit time decay into the ground state sublevels is considered.

The $7S_{1/2}$ state is not allowed to decay directly to the ground state due to selection rules. However, all indirect decay channels via the $6P_{1/2}$ and $6P_{3/2}$ state are allowed. While the decay via the $|6P_{1/2}, F = 4\rangle$ state can be easily included in the simulations, also the other decay channels have to be accounted for. To do so, the combined decay branches via the intermediate states were calculated and a decay of the $7S$ state into the ground state included into the model. While this treatment adequately accounts for pumping effects within the considered level scheme, the population in the dark intermediate states is neglected. All considered decays are illustrated in Fig. 4.3, where the decay via the intermediate dark states is labeled $\Gamma_{6P_{3/2}}$, and Γ_{32} and Γ_{21} represent the total decay rates $\Gamma_{7S_{1/2} \rightarrow 6P_{1/2}}$ and $\Gamma_{6P_{1/2} \rightarrow 6S_{1/2}}$, respectively.

Absorption

In the framework of the semiclassical theory discussed in Sec. 2.4, the absorption coefficient for a two-level system is proportional to $d_{12}\text{Im}\rho_{21}$, where d_{12} is the transition dipole matrix element of the transition and ρ_{21} is the coherence between the two levels.¹ For the discussed level scheme, the different coupling strengths of the magnetic sublevels have to be considered. In this case, the absorption coefficient for the probe transition contains a contribution of all driven transitions of the first excitation step:

$$\alpha \propto \sum d_{ij}\text{Im}\rho_{ji} \equiv \text{Im}\bar{\rho}_{21}. \quad (4.12)$$

Here d_{ij} and ρ_{ji} are the dipole matrix elements and coherences of the corresponding transitions. In the next section, the quantity $\text{Im}\bar{\rho}_{21}$ is used to illustrate the results of the simulations. In order to compare the theoretical results with experimental spectra, the thermal velocity of the atoms has to be taken into account and $\text{Im}\bar{\rho}_{21}$ has to be calculated for all relevant velocity classes. In Eq. 4.12, $\text{Im}\bar{\rho}_{21}$ then has to be substituted by the Doppler-averaged quantity $\text{Im}\bar{\rho}_{d21}$ (see Sec. 2.4).

4.4 Spectroscopic Results

The spectroscopic results presented in the following were obtained with the reference spectroscopy setup described in Sec. 3.4, using the excitation scheme detailed in Sec. 4.1. For all presented measurements, the Rydberg state was $28P_{3/2}$ and the three laser beams were polarized linearly and parallel to each other. As described in the previous section, both the probe laser and the dressing laser were frequency stabilized, while the coupling laser was scanned. The measured spectra thus represent the transmission of the probe laser as a function of the coupling detuning Δ_c . As detailed in the previous section, all Rabi frequencies given were determined using reduced dipole matrix elements.

Fig. 4.4 shows the spectra obtained for three different combinations of the involved Rabi frequencies Ω_p , Ω_d and Ω_c . Also shown are the corresponding velocity-detuning maps of $\text{Im}\bar{\rho}_{21}$ obtained from simulations, based on the theoretical model described in the previous

¹ Note that the tilde on top of the coherence (see Eq. 2.23) is omitted in this expression.

section. Here $\text{Im}\bar{\rho}_{21}$ refers to the coherence between the ground state and the first excited state, averaged over the involved magnetic sublevels. All relevant simulation parameters, including the Rabi frequencies and the quantum numbers of the Rydberg state, were taken to correspond to the experimental situation. In order to compare the simulations with the experimental data, the Doppler-averaged coherence $\text{Im}\bar{\rho}_{d21}$ was fitted to the transmission curves, using the relation (see Sec. 2.4)

$$t = a \cdot \exp(b \text{Im}\bar{\rho}_{d21}). \quad (4.13)$$

Here a and b constitute fitting parameters and the subscript d indicates the Doppler average. The experimental data shown in Fig. 4.4 represents three different regimes in terms of the Rabi frequencies Ω_p , Ω_d and Ω_c . For probe Rabi frequencies Ω_p small in comparison with the dressing Rabi frequency Ω_d (left panel of Fig. 4.4), the dressed states $|d^+\rangle$ and $|d^-\rangle$ are well resolved by the probe laser and the double avoided crossing causes two off-resonant features of enhanced transmission and one absorptive feature on resonance. However, the velocity-detuning map of $\text{Im}\bar{\rho}_{21}$ reveals that the avoided crossings are strongly washed out due to the different coupling strengths of the magnetic sublevels. For large Rabi frequencies Ω_p in comparison with Ω_d (middle panel of Fig. 4.4), power broadening leads to an overlap of the outer wings of the signal and the absorptive feature on resonance shrinks. Eventually, this leads to a Gaussian shaped peak of enhanced transmission on resonance for extremely large Ω_p [61]. If the dressing Rabi frequency Ω_d is increased sufficiently, the different coupling strengths of the magnetic sublevels are directly resolved by the probe laser and a splitting of the outer features of the signal can be observed (right panel of Fig. 4.4).

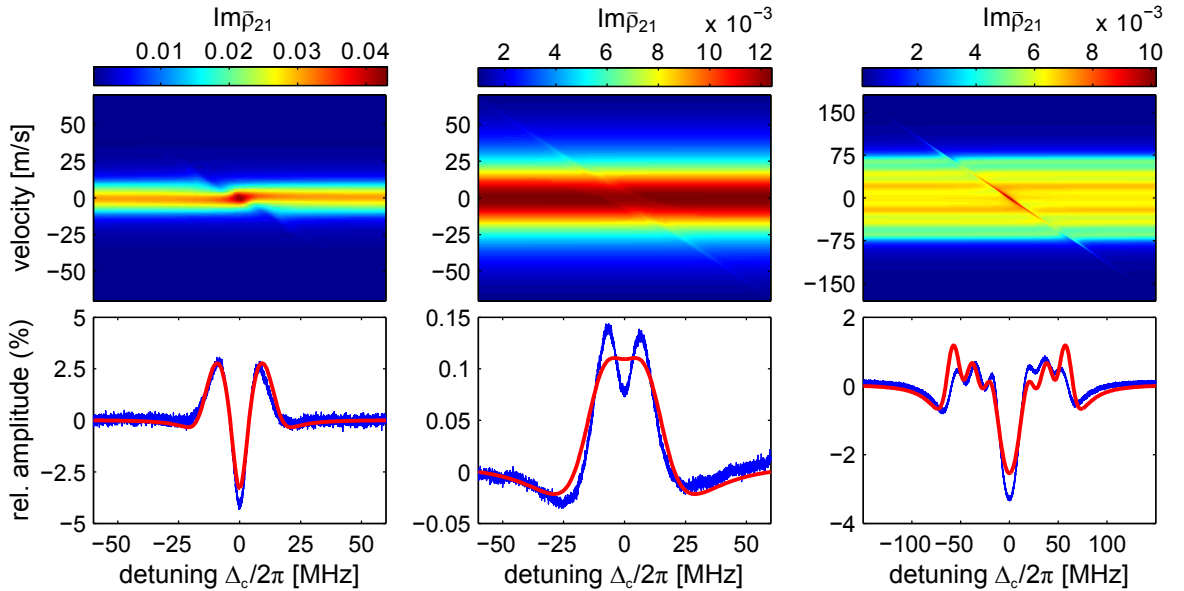


Figure 4.4: Upper half: Simulated coherence between ground state and first excited state, averaged over the involved magnetic sublevels. The result is shown for different velocity classes and coupling laser detunings Δ_c . Lower half: Relative transmission amplitude of the probe laser (with respect to the background absorption). The experimental data (blue, averaged over ten traces) is compared to simulations (red) for Rabi frequencies (left to right) $\Omega_p = 2\pi \times \{5.2, 30.6, 16.6\}$ MHz, $\Omega_d = 2\pi \times \{17, 17, 126\}$ MHz and $\Omega_c = 2\pi \times \{13.8, 13.8, 12.5\}$ MHz.

While the simulations fit qualitatively well to the experimental data, discrepancies are obvious, especially for high probe and dressing Rabi frequencies. At least to some extent, this can be attributed to the Gaussian intensity profile of the laser beams which is not incorporated in the simulations [23]. Additionally, the attenuation of the probe laser over the length of the cell might contribute to the encountered mismatch.

5 Diffusion of Cesium Vapor into Hollow-Core Fibers

For any potential application of vapor-filled hollow-core waveguides (e.g. fibers), the filling process of these waveguides is of special interest. The understanding of the underlying dynamics of this process allows to estimate if the required filling time constitutes a limiting factor for a given experiment or application. In this chapter, a theoretical model for the diffusion of cesium into hollow-core fibers is presented and compared to experimentally measured diffusion curves. The employed model takes the adsorption and desorption of cesium on the fiber walls into account and is based on a treatment described in Ref. [23].

5.1 Theoretical Diffusion Model

The flow dynamics of gases within thin tubes is determined by the dimensionless Knudsen number $Kn = \lambda/d$, where λ is the mean free path length of a molecule or atom in the gas and d is the diameter of the tube. A small Knudsen number $Kn \ll 1$ implies that the gas molecules undergo mainly intermolecular collisions. This hydrodynamic regime is adequately described by the Navier-Stokes equations [63]. By contrast, a large Knudsen number $Kn \gg 1$ corresponds to the free molecular flow regime where the molecules almost exclusively collide with the walls of the tube. In this case, it was shown that the dynamics can be described as a one dimensional diffusion process [63–65].

The mean free path length of cesium atoms in a thermal vapor at pressures corresponding to the vapor pressure $p_v(T)$ (see Sec. 2.1) is given by [63]

$$\lambda = \frac{k_B T}{\sqrt{2} \pi d_a^2 p_v(T)}. \quad (5.1)$$

Here k_B is the Boltzmann constant, T is the temperature and $d_a = 5.9 \text{ \AA}$ is the atomic diameter of cesium [66]. For a temperature of 45°C (which was approximately the temperature of the cesium reservoir in the diffusion measurement described later), Eq. 5.1 gives a mean free path length of $\lambda \approx 2 \text{ m}$ which corresponds to Knudsen numbers of $Kn > 10^4$ for typical fiber diameters on the micrometer length scale. For the conditions present in our experiment, the migration of cesium vapor into hollow-core fibers therefore takes place in the free molecular flow regime and can be described with the one dimensional diffusion equation [67]

$$\frac{\partial n}{\partial t} = D \frac{\partial^2 n}{\partial x^2}. \quad (5.2)$$

Here $n(x, t)$ is the atomic number density at the space coordinate x and time t , and D is the diffusion constant. For the diffusion of cesium vapor in hollow-core fibers, the diffusion constant does not only depend on the ambient temperature and the geometry of the fiber

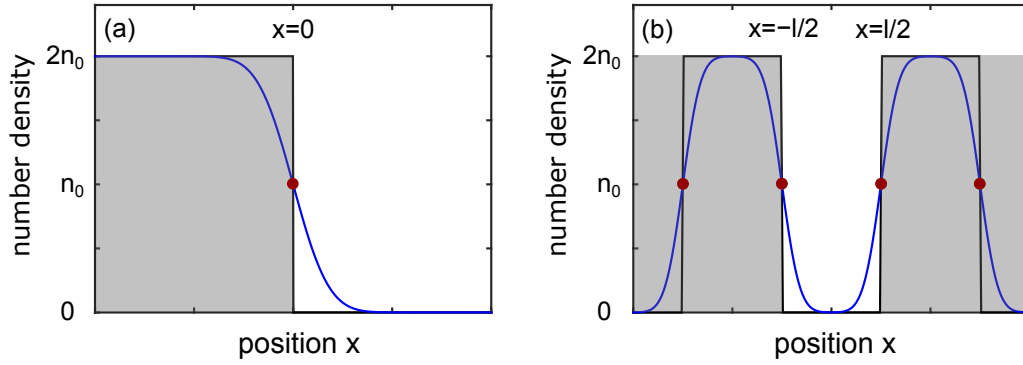


Figure 5.1: Illustration of two solutions of the diffusion equation (see Eq. 5.2) for constant boundary conditions (marked as red dots). (a) The complementary error function in Eq. 5.6 fulfills the boundary condition $n(x = 0, t) = n_0$. (b) For the boundary conditions $n(x = \pm l/2, t) = n_0$, a solution can be found in terms of a superposition of complementary error functions (see Eq. 5.7).

but also on adsorption and desorption processes of cesium on the fiber walls [23]. For a thin tube, Ref. [68] gives a diffusion constant of

$$D = \frac{4}{3} \frac{r^2}{\tau + (2r/\bar{v})}. \quad (5.3)$$

Here r is the radius of the tube and $\bar{v} = \sqrt{8k_B T / (\pi m)}$ is the mean velocity of the gas atoms with mass m .¹ The adsorption time τ can be interpreted as the mean time an atom stays at the fiber wall after a collision. For a given wall temperature T_w , the adsorption time is expected to be given by [66, 69]

$$\tau = \tau_0(\theta) \exp\left(\frac{E_a(\theta)}{k_B T_w}\right), \quad (5.4)$$

where the characteristic time τ_0 and the adsorption energy E_a are functions of the surface coverage θ .

In the diffusion measurement presented in Sec. 5.2, the temperatures of the reservoir and of the rest of the chamber were approximately $T_{\text{res}} = 45^\circ\text{C}$ and $T_c = 80^\circ\text{C}$ respectively. Due to this large temperature difference, the surface coverage θ can be expected to be low.² It therefore seems reasonable to assume no interactions between individual adsorbed cesium atoms and to assume D to be a constant. In this case, Eq. 5.2 becomes a linear second order partial differential equation which is identical to the one dimensional heat equation. The solutions of the diffusion equation depend on the boundary conditions of a given problem and can often be found with the method of separation of variables or by a Laplace transform [67]. In our experimental setup (see Sec. 3.2), the fibers are mounted inside a vacuum chamber and as soon as the cesium vapor was released into the chamber, it diffused from both ends of the fibers into the open core. If the vacuum chamber is assumed to constitute an infinite

¹ An expression which deviates slightly from the one given in Eq. 5.3 is derived in Ref. [64].

² Based on an estimation given in Ref. [66], the surface coverage is below the one percent level for the considered temperatures.

reservoir of cesium vapor at a constant number density n_0 and the length of a specific fiber is l , the boundary conditions corresponding to the experimental situation can be written as

$$\begin{aligned} n(x, t = 0) &= 0, & -l/2 < x < l/2, \\ n(x = l/2, t) &= n(x = -l/2, t) = n_0. \end{aligned} \quad (5.5)$$

To find a solution for these boundary conditions, it is beneficial to first consider the case of a semi-infinite medium which extends from $x = 0$ to $x = \infty$ for the boundary conditions $n(x > 0, t = 0) = 0$ and $n(x = 0, t) = n_0$. The well-known solution of this problem is given by [67]

$$n(x, t) = n_0 \operatorname{erfc} \frac{x}{2\sqrt{Dt}}, \quad (5.6)$$

where the complementary error function is defined as $\operatorname{erfc}(x) = 1 - \operatorname{erf}(x)$ (see Fig. 5.1). The solution for the originally considered boundary conditions given in Eq. 5.5 can then be found as a superposition of solutions of the semi-infinite case:

$$n(x, t) = n_0 \sum_{q=0}^{\infty} (-1)^q \operatorname{erfc} \frac{x + (2q+1)l/2}{2\sqrt{Dt}} + n_0 \sum_{q=0}^{\infty} (-1)^q \operatorname{erfc} \frac{-x + (2q+1)l/2}{2\sqrt{Dt}}. \quad (5.7)$$

An illustration showing that this expression leads to a constant density of n_0 at $x = \pm l/2$ is shown in Fig. 5.1. The density profile inside the fiber predicted by Eq. 5.7 is shown in Fig. 5.2 for different values of the dimensionless time $t_r = Dt/l^2$. Also shown is the filling factor \bar{n}/n_0 , where \bar{n} is the mean density in the fiber. Following the definition given in Ref. [23], the filling time of a fiber is defined in the following as the duration after which the

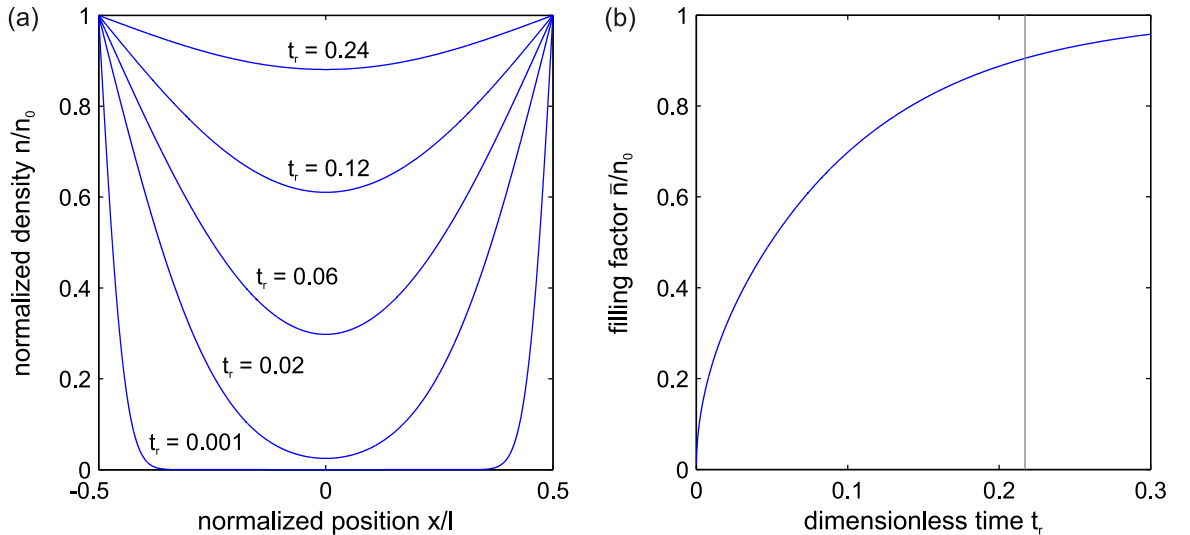


Figure 5.2: Diffusion into a hollow-core fiber of length l as predicted by Eq. 5.7. The infinite series was truncated at $q = 100$. Shown are normalized quantities and time is given as a dimensionless variable $t_r = Dt/l^2$. (a) Spatial density profile at different dimensionless times t_r . The fiber ends at $x = -l/2$ and $x = l/2$ are held at constant density n_0 . (b) Filling factor \bar{n}/n_0 as a function of t_r . The filling time $t_{85\%}$ as defined in the text is marked as a grey line.

atomic number density at every position of the fiber exceeds 85 % of n_0 . With Eq. 5.7, the filling time for a given diffusion constant and fiber length can be approximated to be

$$t_{85\%} \approx 0.217 \frac{l^2}{D}. \quad (5.8)$$

In terms of the dimensionless time introduced previously, the filling time is therefore $t_{85\%} = 0.217$. Even if for most applications the filling process seems more important than the venting process, it should be mentioned that the venting process is complementary to the filling process in the free molecular flow regime [63]:

$$n_{\text{vent}}(x, t) = 1 - n_{\text{fill}}(x, t). \quad (5.9)$$

5.2 Experimental Results

Since the absorption coefficient α of a ground state transition is directly proportional to the atomic number density n of a vapor, optical density (OD) measurements can be utilized to determine the density of a uniform vapor (see Sec. 2.4). In case of a partly vapor-filled fiber, the optical density is proportional to the filling factor \bar{n}/n_0 which implies that absorption spectroscopy can be used to measure the diffusion of an atomic vapor into a fiber. Following this strategy, the 895 nm probe beam was coupled into the 85 mm long 60 μm kagome fiber (coupling efficiency $\sim 57\%$) mounted in the CF40 cube (see Sec. 3.2). The filling was then monitored by scanning the laser over all four absorption dips of the D_1 line (see Sec. 4.1) continuously. At the same time, the optical density in the chamber around the fiber was probed with a freespace beam. The optical density was then extracted from the measured data by fitting a theoretical absorption profile to the spectra [70]. As an example, a fitted spectrum is shown as inset in Fig. 5.3. The laser power (measured at the output end of the fiber and before it was exposed to cesium) was $p_{895} = 40 \text{ nW}$. Inside the fiber, this corresponds to light intensities below the saturation intensity.

When the cesium ampule inside the flexible metal bellow was broken (see Sec. 3.2), both chamber and reservoir were held at room temperature. Although, this approach omits inaccurate temperature measurements of the system, it was discarded, since no cesium could be detected in the main chamber after one day. Reservoir and chamber were subsequently heated to approximately $T_{\text{res}} = 45^\circ\text{C}$ and $T_c = 80^\circ\text{C}$ respectively. The measured time evolution of the optical density after the heating was switched on is shown in Fig. 5.3. In both the fiber and the chamber, no cesium could be detected for over 10 hours. After the first detection of cesium, the optical density however increased rapidly within the chamber and saturated around three days after the heating was switched on. The delayed appearance of cesium vapor in the chamber can most probably be attributed to the deposition of cesium on the stainless steel walls of the vacuum chamber [71]. Such a coating process is expected to prohibit a pressure build-up in the chamber, until the walls are saturated.

From Fig. 5.3 it is apparent that even after a filling time of 400 hours, the optical density in the fiber did not reach the value measured in the chamber. To get a rough estimate of the corresponding diffusion constant D , the filling curve was compared to the theoretical model introduced in Sec. 5.1. A reasonable agreement between experiment and theory could be found for a diffusion constant of $D_{\text{est}} = 8 \times 10^{-10} \text{ m}^2/\text{s}$ and an optical density in the chamber of $OD_{\text{freespace}} = 35$ (see dashed line in Fig. 5.3). To account for the delayed appearance of

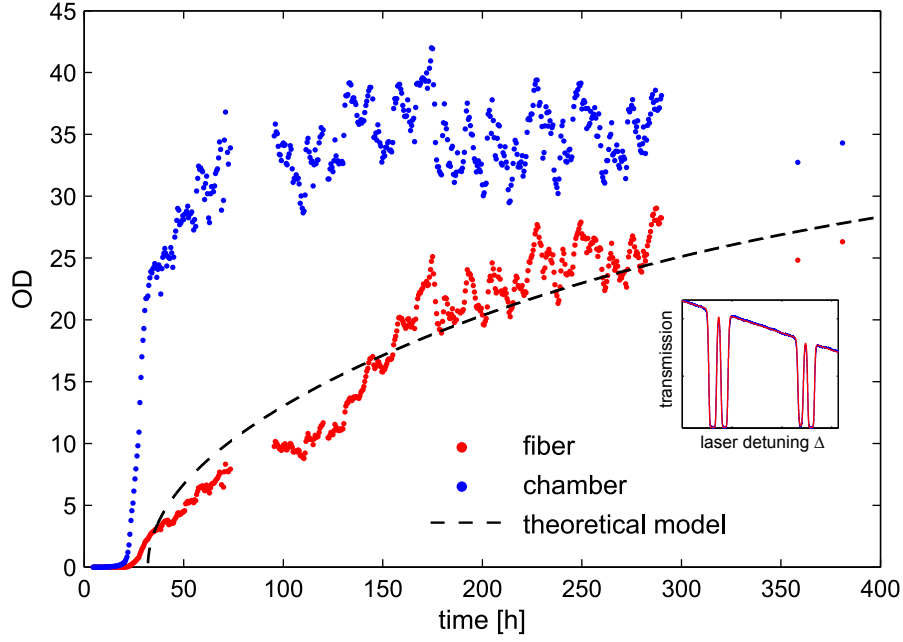


Figure 5.3: Measured time evolution of the OD in vacuum chamber and 85 mm long 60 μm kagome fiber. At $t = 0$ h, reservoir and chamber were heated to approximately $T_{\text{res}} = 45^\circ\text{C}$ and $T_c = 80^\circ\text{C}$ respectively. Dashed line: theoretical model (see Eq. 5.7) for $D_{\text{est}} = 8 \times 10^{-10} \text{ m}^2/\text{s}$ and $OD_{\text{freespace}} = 35$. The time axis was shifted in the theoretical model by 32 hours to account for the delayed appearance of cesium in the chamber which can be attributed to the deposition of cesium on the stainless steel walls of the chamber. The OD was extracted by fitting a theoretical absorption profile to the spectra. The inset shows an exemplary spectrum (blue, averaged seven times) and the fit (red).

cesium, the time axis in the theoretical model was shifted by 32 hours. Since the optical density in the chamber reached equilibrium on a much faster time scale than in the fiber, the error introduced by assuming constant boundary conditions in the theoretical model can be expected to be small.

According to Eq. 5.3, the diffusion constant D_{est} corresponds to an adsorption time of $\tau_{\text{est}} \approx 1.5 \text{ s}$ which can be used to compare the given estimate with results of adsorption time measurements. The factor τ_0 and the adsorption energy E_a which determine the adsorption time τ (see Eq. 5.4) are given in Refs. [66, 69] for the case of cesium atoms adsorbing on quartz glass.¹ The adsorption times corresponding to these values are directly compared to the estimate τ_{est} in Table 5.1. To illustrate the influence of the adsorption time on the diffusion process, also the corresponding diffusion constants according to Eq. 5.3 and filling times $t_{85\%}$ according to Eq. 5.8 are given for the conditions present in our experiment. It is apparent that the given adsorption times are not compatible with each other and differ orders of magnitude from each other. It is important to note that all three values of τ were measured with different methods. While τ was roughly estimated from a diffusion curve in this work, surface conductivity measurements and evanescent spectroscopy were employed in Ref. [66] and Ref. [69] respectively. The encountered discrepancy might therefore be a result of different theoretical models used to extract the adsorption time from the experimental

¹ The inner walls of the kagome fiber are made of quartz glass.

τ_0 [s]	E_a [eV]	corr. τ [s]	corr. D [m ² /s]	corr. $t_{85\%}$ [h]	reference
-	-	1.5	$8 \cdot 10^{-10}$	544	this work
10^{-13}	0.66 ± 0.05	$2.6 \cdot 10^{-4}$	$4.6 \cdot 10^{-6}$	0.095	Ref. [66]
10^{-8}	0.2	$7.1 \cdot 10^{-6}$	$1.6 \cdot 10^{-4}$	0.0027	Ref. [69]

Table 5.1: Comparison of the estimated adsorption time τ_{est} with values calculated with Eq. 5.4 and E_a and τ_0 taken from Refs. [66, 69]. To illustrate the influence of the adsorption time on the diffusion process, the corresponding diffusion constant D and filling time $t_{85\%}$ for the experimental circumstances in our experiment are given.

results. This also raises the question about the validity of the treatment introduced in Sec. 5.1. Additionally, the exact conditions of the studied surfaces are expected to have a strong influence on the adsorption time. This includes impurities on the surface and especially the duration how long the surface was exposed to cesium. The latter point was shown to be crucial and suggests a migration of cesium atoms into the quartz on the order of a few atomic diameters [69]. The different adsorption times might therefore also be attributed to different experimental circumstances.

The evolution of the optical density shown in Fig. 5.3 exhibits strong fluctuations for both, the fiber and the freespace case. A striking feature of the curves is, that the fluctuations in fiber and chamber seem to be correlated. Since the beam powers were found to be stable, this behavior can not be attributed to saturation effects. To examine if the optical density variations are temperature induced, the temperature of the vacuum chamber was actively modulated after the diffusion measurement presented above was completed. The temperature of the reservoir was not changed. Fig. 5.4 shows the temporal evolution of the chamber temperature (measured with a Pt100 temperature sensor fixed to the outside of the chamber) and the optical density measured in chamber and fiber. The data qualitatively reveals a strong

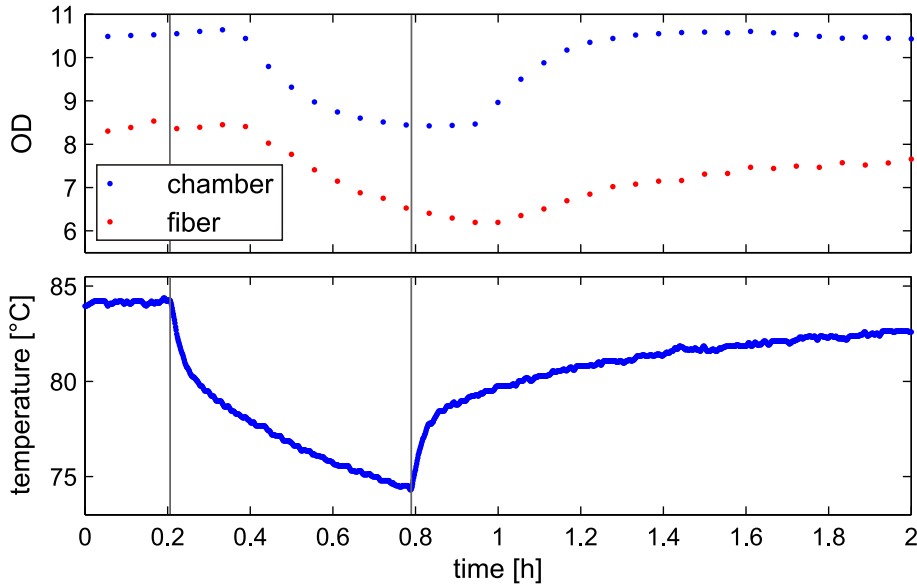


Figure 5.4: Short-term influence of the chamber temperature on the OD in chamber and fiber. The strong temperature dependence of the OD can be attributed to the temperature dependent adsorption process of cesium on the chamber and fiber walls (see Eq. 5.4).

short-term influence of the chamber temperature on the optical density in the chamber as well as in the fiber. The decrease of optical density with decreasing temperature is consistent with Eq. 5.4 which predicts more atoms to be adsorbed on chamber and fiber walls for lower temperatures. While the evolution of the optical density is delayed with respect to the temperature curve, this can be explained by the heat transfer between the outside and the inside of the vacuum chamber. Given the strong temperature dependence observed in this measurement, it seems likely that the fluctuations observed in the diffusion measurement were caused by temperature variations in the laboratory which were determined to be on the order of a few degrees Celsius. It should be noted that the optical density in the temperature measurement presented here, is much lower than in the case of the diffusion measurements, despite the fact that the heating of the reservoir was not changed. This suggests either a temporary failure of the reservoir heating (which later failed completely) or the sudden appearance of a presumably virtual leak. The possibility of a contamination during the temperature measurements can therefore not be excluded. However, it seems unlikely that this would have influenced the qualitative behavior of the system.

6 Spectroscopy in Hollow-Core Fibers

Rydberg excitation in hollow-core fibers was first demonstrated in 2014 in our institute [23, 24]. As in the work described here, thermal cesium vapor was used and main quantum numbers up to $n = 40$ and $n = 30$ were reached in kagome-type hollow-core photonic crystal fibers with core diameters of $60\text{ }\mu\text{m}$ and $19\text{ }\mu\text{m}$ respectively. In this chapter, spectroscopic results obtained in the new experimental setup (see Ch. 3) are presented. To study the impact of the confining environment of hollow-core fibers on Rydberg atoms under different experimental conditions, spectra were measured at different temperatures, optical densities and probe laser powers. The spectra were then compared to reference spectra simultaneously obtained in a vapor cell.

6.1 Guiding Properties

For our investigations, we focused on two kagome fibers with core diameters of $60\text{ }\mu\text{m}$ and $12\text{ }\mu\text{m}$ and a bandgap fiber with a core diameter of $12\text{ }\mu\text{m}$ (see Ch. 3). The $12\text{ }\mu\text{m}$ fibers were chosen since the achievement of Rydberg excitation in such small fiber cores would constitute a major step towards the study of Rydberg-induced optical nonlinearities.

The employed Rydberg excitation scheme detailed in Sec. 4.1 is based on a three-photon transition at the wavelengths 895 nm , 1359 nm and 780 nm . Unexpectedly, it was found that the kagome fiber does not guide at 1359 nm at all and is therefore inadequate for the used excitation scheme. The bandgap fiber (see Fig. 6.1a) was found to guide a small part of the incoupled 1359 nm light in the fundamental mode before the fiber was exposed to cesium vapor (see Fig. 6.1c). After several weeks of exposure to cesium however, the fiber did not guide at 1359 nm anymore and showed a strongly reduced guidance at 780 nm . Similar observations are described in Ref. [72], where rubidium was shown to alter the guidance properties of a bandgap fiber. As a consequence, the $60\text{ }\mu\text{m}$ kagome fiber which guides well at all three excitation wavelengths was used for all measurements carried out in the CF40-chamber. An image of the fundamental mode of the probe beam in the $60\text{ }\mu\text{m}$ kagome fiber is shown in Fig. 6.1d.

6.2 Spectroscopic Results

As presented in the following, the Rydberg spectra measured in the employed hollow-core fibers show line shifts and lineshape distortions with respect to simultaneously taken spectra in a reference cell. Line shifts of Rydberg signals in hollow-core fibers were previously found and mainly attributed to static electric fields inside the fibers [23, 24]. These shifts were shown to vanish after exposing the fibers long enough to cesium. In the experiment described here, it was found that in addition to the exposure time of the fibers to cesium, also the chamber temperature has great influence on the lineshape of the spectroscopy signal. Fig. 6.3a shows

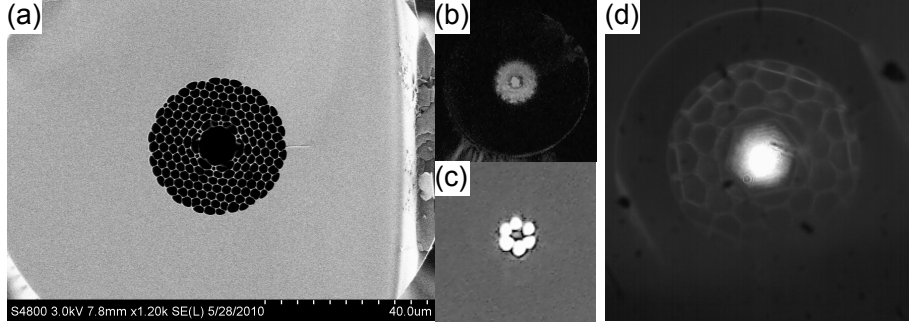


Figure 6.1: (a)-(c) Employed 12 μm bandgap fiber. (a) SEM image (provided by the Max Planck Institute for the Science of Light – Russell division, Erlangen). Also shown is the mode of 895 nm (b) and 1359 nm (c) light before the fiber was exposed to cesium. While a small fraction of the 1359 nm light was guided in the fundamental mode before the fiber was exposed to cesium, the guiding was lost in a cesium atmosphere. (d) Fundamental mode at 895 nm in the 60 μm kagome fiber guiding well at all three excitation wavelengths.

two spectra (see Ch. 4) obtained at different chamber temperatures T_{ch} and a constant reservoir temperature of $T_{\text{res}} = 22^\circ\text{C}$. Both spectra were measured more than six months after the cesium reservoir was broken in the 60 μm kagome fiber mounted in the CF40-chamber (see Sec. 3.2). The chamber had been heated continuously since the fibers were exposed to cesium and the optical density inside fiber and surrounding chamber was measured at the chamber temperature $T_{\text{ch}} \approx 63^\circ\text{C}$ to be $OD_{\text{kagome}} = 2$ and $OD_{\text{chamber}} = 2.6$ respectively. The optical density of the short segments between the fiber ends and the vacuum windows was determined to be $OD_{\text{cladding}} \approx 0.09$ by coupling the probe laser into the cladding of the fiber. The spectroscopy signal originating from outside the fiber is therefore expected to be very small. Since the lineshape of the three-photon signal was found to be heavily deformed at chamber temperatures higher than the reservoir temperature (see upper spectrum in Fig. 6.3a), the chamber was cooled down to room temperature (22°C). The corresponding spectrum in Fig. 6.2a was measured one day after the cool-down process and exhibits only a slight deformation. Figure 6.2b shows a probe spectrum measured after the chamber was held at room temperature for one month. As a comparison, also a simultaneously taken reference spectrum (measured in the reference cell, see Sec. 3.4) is shown. All Rabi frequencies in reference cell and fiber were comparable. While the spectrum taken in the fiber does not exhibit severe lineshape distortions, it is clearly visible that the spectroscopic signal is broadened and shifted slightly with respect to the reference spectrum.

Considering the results presented above and the findings of previous work [23, 24], it seems reasonable to attribute the observed lineshape deformations to inhomogeneous electric fields inside the fiber. To see, that this explanation is in agreement with the vanishing lineshape deformation at low chamber temperatures, the adsorption of cesium atoms on the glass walls of the fiber has to be considered. As discussed in Ch. 5, the surface coverage of cesium atoms on the glass is expected to increase with decreasing temperature. Such an increase in surface coverage was shown to be accompanied by an increasing electrical conductivity of the surface layer in Ref. [66]. The charges causing the assumed electric field could therefore drain off more easily at low temperatures. While the observed lineshape deformations might be explainable by an inhomogeneous field alone, results presented in the following suggest

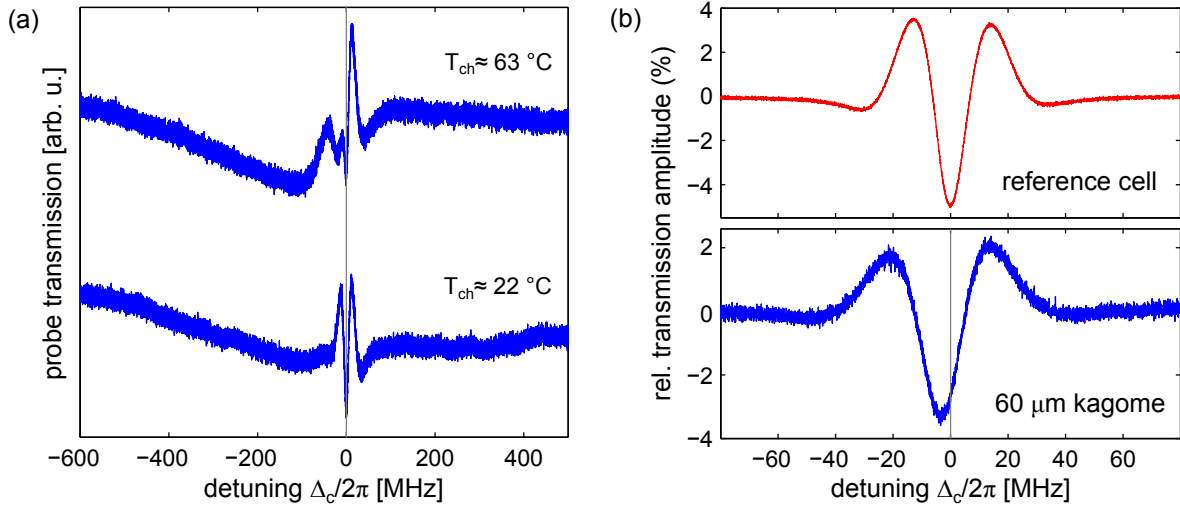


Figure 6.2: Probe spectra obtained in the 60 μm kagome fiber exposed more than six months to cesium for the Rydberg state $28P_{3/2}$. (a) Spectra (averaged 500 times) for different chamber temperatures T_{ch} and constant reservoir temperature $T_{\text{res}} = 22^\circ\text{C}$. The lineshape of the upper spectrum is severely deformed. The zero point of the frequency axis (marked by grey line) was determined from a reference spectrum. The beam powers (measured at off-resonant frequencies after the fiber) were $p_p = 0.4 - 0.5 \mu\text{W}$, $p_d = 4.86 \mu\text{W}$ and $p_c = 18 - 20 \text{ mW}$ for probe, dressing and coupling beam respectively. (b) Spectrum (averaged 500 times) obtained one month after the chamber was cooled down to room temperature. Also shown is a spectrum obtained simultaneously in the reference cell for comparable Rabi frequencies. The beam powers were $p_p = \{0.1, 0.75\} \mu\text{W}$, $p_d = \{4.8, 60\} \mu\text{W}$ and $p_c = \{3.55, 38\} \text{ mW}$ for fiber and reference cell respectively. The OD in chamber and kagome fiber was measured to be $OD_{\text{chamber}} = 2.2$ and $OD_{\text{kagome}} = 1.1$.

that the Rydberg population has a significant influence on the electric field experienced by the atoms in the fiber. The encountered lineshapes might therefore be the result of a local electric field which is influenced by the coupling laser detuning Δ_c .

To gain a better understanding of the observed line shifts and deformations, also spectra obtained with the 60 μm kagome fiber and 60 μm capillary mounted in the e-chamber (see Sec. 3.3) were compared to reference spectra. In contrast to the measurements presented above, the fibers were only exposed for two months to cesium and both reservoir and chamber were heated ($T_{\text{res}} \approx 45^\circ\text{C}$, $T_{\text{ch}} \approx 90^\circ\text{C}$). The measured optical densities for the kagome fiber ($OD_{\text{kagome}} = 8.6$) and for the capillary ($OD_{\text{capillary}} = 11$) are both smaller than the optical density measured in the chamber ($OD_{\text{chamber}} = 19.5$). As discussed in Ch. 5, this indicates that the diffusion process of the cesium atoms into the fibers had not reached equilibrium at the time of the measurements. For both fibers no severe lineshape deformations were observed. Given the fact that the chamber temperature was higher than the reservoir temperature, this seems to be inconsistent with the results presented previously. However, it is important to note again that the optical density was much higher than in the previously considered case and that the fibers were exposed for only two months to cesium. Although no severe lineshape distortions were found, a clear shift of the signal with respect to a simultaneously taken reference signal could be observed. As an example, a probe spectrum obtained with the 60 μm kagome fiber is shown in Fig. 6.3a. Strikingly, an influence of the probe laser power on the shift was found for both, the kagome fiber and the capillary. In

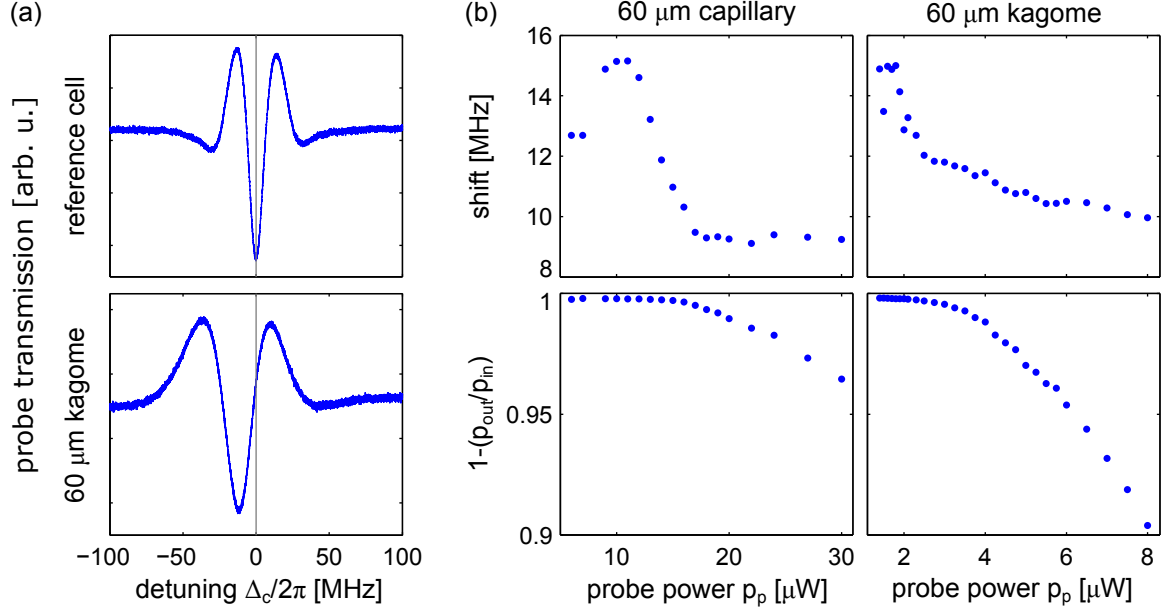


Figure 6.3: Line shifts observed at high optical densities ($OD_{\text{kagome}} = 8.6$, $OD_{\text{capillary}} = 11$) for the Rydberg state $28P_{3/2}$. (a) Spectrum in 60 μm kagome fiber and simultaneously taken reference spectrum. Beam powers: $p_p = \{2, 3\} \mu\text{W}$, $p_d = \{67, 8.2\} \mu\text{W}$ and $p_c = \{6, 8.9\} \text{mW}$ for reference cell and fiber respectively. (b) Dependence of the line shift on the probe power p_p (upper panel) for p_d and p_c as in (a). As a measure of the saturation of the probe transition, the absorbed fraction of the probe power is plotted in the lower panel. p_{out} was estimated from a photodiode signal.

Fig. 6.3b (upper panel), the encountered line shifts are plotted as a function of the probe power p_p for the Rydberg state $28P_{3/2}$. Both, the data obtained with the kagome fiber and with the capillary qualitatively show a decrease of the shift with increasing probe power. It is worth to note that the largest gradient in the shown curves appears at the transition from unsaturated absorption to saturated absorption of the atomic ensemble. As a measure of the saturation, the absorbed fraction of the probe power ($1 - p_{\text{out}}/p_{\text{in}}$) is shown in the lower panel of Fig. 6.3b. While the distinct behavior of the shift remains unexplained (e.g. the probe dependence at low p_p in the capillary, see Fig. 6.3b), the curves suggest that the increasing Rydberg population which is associated with increasing probe power has a significant influence on the system.

In summary, the observed lineshape deformations and shifts indicate the influence of a local electric field on the atoms inside the fibers. While the origin of the electric charges causing this field is not known, it is promising that the encountered deformations vanish at low fiber temperatures and the line shifts were shown to disappear if the fibers are exposed to cesium long enough [24].

7 Rf Dressing of the Rydberg State

The experimental apparatus described in Sec. 3.3 allows for the application of radio-frequency (rf) electric fields to individual segments of a hollow-core fiber. In this chapter, experimental results are presented and compared to a theoretical model which describes the action of an ac electric field on Rydberg atoms. As detailed in the following, the experimental setup was used to gain a spatial resolution of the spectroscopy signal along the fiber and to study the formation of rf-induced sidebands of the Rydberg state.

7.1 Theoretical Framework

This section discusses the theoretical framework later used to interpret the experimental spectra of rf-dressed Rydberg atoms. Due to the small polarizability of the lower three states of the excitation scheme (see Sec. 4.1) on the order of $\text{Hz}/(\text{Vcm}^{-1})^2$ [31, 73], the influence of the considered electric fields on these states can be safely neglected. The Rydberg state, however, is highly sensitive to external fields since the polarizability α scales with the effective principal quantum number to the power of seven (see Sec. 2.2). For the $30P_{3/2}$ state for example, the scalar polarizability was experimentally determined to be $\alpha_0 = 24.57 \text{ MHz}/(\text{Vcm}^{-1})^2$ [35]. The theoretical treatment presented in this chapter describes the action of a rf field on the Rydberg state and is based on a Floquet approach employed in Ref. [29]. Very similar descriptions can also be found in Refs. [5, 27, 30, 62].

The Hamiltonian of the considered system can be written as $H = H_a + H_{\text{ef}}$, where H_a is the Hamiltonian of the unperturbed atom and H_{ef} contains the interaction with the electric field. If we account for a dc offset and assume the field modulation to be sinusoidal (as in the measurements described later), we can write the rf field as

$$\mathbf{E}(t) = \mathbf{E}_{\text{dc}} + \mathbf{E}_{\text{ac}} \cos \omega t. \quad (7.1)$$

For modulation frequencies ω much smaller than all relevant transition frequencies in the system, the electric field can be treated as quasi-static. If the field is sufficiently weak, perturbation theory is applicable and the Rydberg state exhibits the quadratic Stark effect discussed in Sec. 2.3. The energy shift caused by the electric field can be written as

$$\varepsilon_{\text{ef}} = -\frac{1}{2}\alpha E^2 = -\frac{1}{2}\alpha \left[E_{\text{dc}}^2 + \frac{1}{2}E_{\text{ac}}^2 + 2E_{\text{dc}}E_{\text{ac}}\cos \omega t + \frac{1}{2}E_{\text{ac}}^2\cos 2\omega t \right], \quad (7.2)$$

where α is the polarizability of the Rydberg state and we assume the dc field and the ac field to be collinear. In order to solve the time-dependent Schrödinger equation

$$i\hbar \frac{\partial \Psi}{\partial t} = H\Psi, \quad (7.3)$$

we separate the wave function of the considered state into a spatial and a temporal part. While this is in general not permissible for a time-dependent problem, it was shown in Ref. [29]

that the spatial dependence of the wave function remains to a good approximation unaltered under the action of the external fields considered here. We can thus write

$$\Psi(\mathbf{r}, t) = \psi(\mathbf{r})\Phi(t), \quad (7.4)$$

where $\psi(\mathbf{r})$ is a stationary state of the static part H_s of the Hamiltonian [27]. From Eq. 7.2 we can see, that H_s does not only include the atomic Hamiltonian H_a and a part accounting for the dc field, but also a contribution caused by the ac field. With the energy ε_0 of the unperturbed state and the definition

$$H_s\psi(\mathbf{r}) = \left[\varepsilon_0 - \frac{1}{2}\alpha(E_{dc}^2 + \frac{1}{2}E_{ac}^2) \right] \psi(\mathbf{r}) = \varepsilon_s\psi(\mathbf{r}), \quad (7.5)$$

the Schrödinger equation takes the form

$$i\hbar\psi(\mathbf{r})\frac{\partial\Phi(t)}{\partial t} = \left[\varepsilon_s - \alpha E_{dc}E_{ac}\cos\omega t - \frac{1}{4}\alpha E_{ac}^2\cos 2\omega t \right] \psi(\mathbf{r})\Phi(t). \quad (7.6)$$

We can now eliminate $\psi(\mathbf{r})$ and obtain the temporal part of the wave function $\Phi(t)$ by integrating the differential equation. This yields

$$\begin{aligned} \Phi(t) &= \exp\left(-\frac{i}{\hbar}\int\left[\varepsilon_s - \alpha E_{dc}E_{ac}\cos\omega t - \frac{1}{4}\alpha E_{ac}^2\cos 2\omega t\right]dt\right) \\ &= \exp\left(-\frac{i}{\hbar}\varepsilon_s t\right)\exp\left(\frac{i\alpha E_{dc}E_{ac}}{\hbar\omega}\sin\omega t\right)\exp\left(\frac{i\alpha E_{ac}^2}{8\hbar\omega}\sin 2\omega t\right). \end{aligned} \quad (7.7)$$

A more instructive representation of this result can be obtained by employing the Jacobi-Anger expansion [74]

$$\exp(i\varphi\sin\theta) = \sum_{n=-\infty}^{\infty} \exp(in\theta)J_n(\varphi), \quad (7.8)$$

in order to expand Eq. 7.7 in terms of Bessel functions J_n . If we expand both appropriate exponential functions and additionally define the variables

$$x = \frac{\alpha E_{dc}E_{ac}}{\hbar\omega} \quad \text{and} \quad y = \frac{\alpha E_{ac}^2}{8\hbar\omega} \quad (7.9)$$

connected to a modulation at ω and 2ω respectively (see Eq. 7.7), the full wave function including the spatial dependent part becomes

$$\Psi(\mathbf{r}, t) = \psi(\mathbf{r})\exp\left(-\frac{i}{\hbar}\varepsilon_s t\right)\sum_{n=-\infty}^{\infty}\exp(in\omega t)\sum_{m=-\infty}^{\infty}J_{n-2m}(x)J_m(y). \quad (7.10)$$

For the further analysis, it is helpful to rewrite Eq. 7.10 in a slightly different form by introducing the coefficients

$$A_n(x, y) = \sum_{m=-\infty}^{\infty} J_{n-2m}(x)J_m(y), \quad (7.11)$$

later shown to characterize the spectra of rf-dressed Rydberg states. The resulting representation

$$\Psi(\mathbf{r}, t) = \sum_{n=-\infty}^{\infty} A_n(x, y)\exp\left(-\frac{i}{\hbar}\varepsilon_s t + in\omega t\right)\psi(\mathbf{r}) \quad (7.12)$$

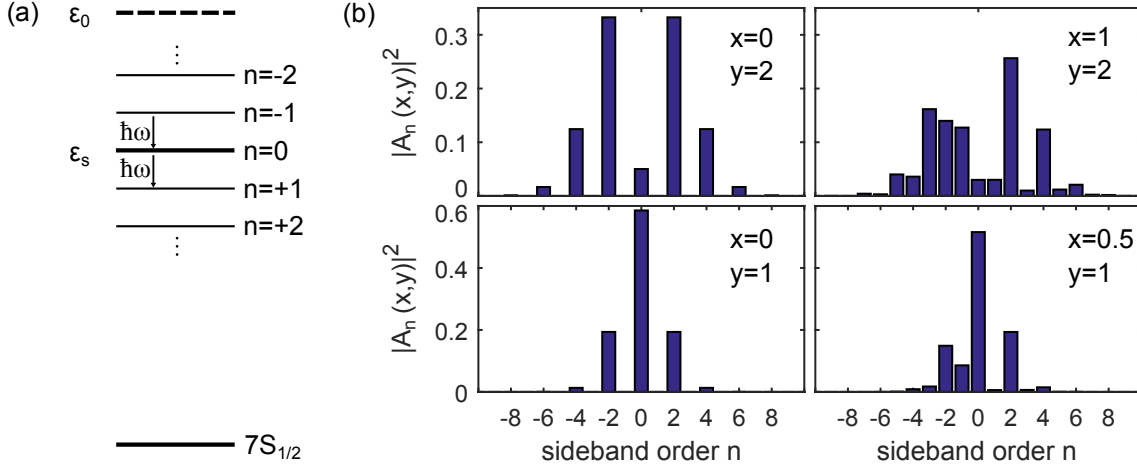


Figure 7.1: (a) Under the action of a rf electric field, the Rydberg state turns into a manifold of Floquet states. Even if no dc field is present, the carrier state ($n = 0$) is Stark-shifted with respect to the original unperturbed state at an energy of ϵ_0 . (b) Sideband amplitudes $|A_n(x, y)|^2$ for different values of x and y . For $x = 0$ (no dc field), odd-order sidebands are forbidden and the spectrum is symmetric. With increasing field amplitude more sidebands are populated. For $x \neq 0$, also odd-order sidebands are allowed and the spectrum gets asymmetric.

suggests two effects of the electric field on the bare atomic state. Firstly, the original state is shifted in energy by $\epsilon_s - \epsilon_0 = -1/2 \alpha E_{dc}^2 - 1/4 \alpha E_{ac}^2$. While the first term of this expression corresponds to the quadratic Stark effect induced by the dc field, the second term corresponds to a dc-like shift induced by the ac field which scales quadratic with the root mean square of the field amplitude. Secondly, Eq. 7.12 suggests the formation of an infinite number of sidebands separated by energies $n\hbar\omega$ from the carrier state with an energy of ϵ_s (see Fig. 7.1a). Since the Bessel functions in $A_n(x, y)$ approach zero for large n and arguments smaller than $|n|$, only a limited number of these Floquet states significantly contribute to the wave function [5]. Already from Eq. 7.2 it is obvious, that an energy modulation at the driving frequency ω only occurs if a dc electric field is present. As a consequence, no odd-order sidebands exist without dc field.

In the experiment described in this thesis, the Rydberg state is excited from the $7S_{1/2}$ state by means of a scanning coupling laser. In this case, the sidebands predicted by Eq. 7.12 occur in the probe spectrum (see Sec. 4.1) and can be interpreted as multiphoton excitation processes involving one laser photon and n rf photons. For red detunings of the coupling laser with respect to the Stark-shifted Rydberg state, these excitations can be attributed to the absorption of one laser photon and one or more rf photons. Excitations occurring at blue detunings of the coupling laser correspond to the absorption of one laser photon and the stimulated emission of one or more rf photons. Since the probability to excite the n -th sideband is proportional to $|A_n(x, y)|^2$, this factor is expected to reflect the relative magnitude of this specific sideband in the spectrum [27]. The sideband amplitudes $|A_n(x, y)|^2$ are illustrated for four exemplary values of x and y in Fig. 7.1b. If no dc field is present, x is zero and the amplitudes $|A_n(x, y)|$ of the sidebands do not depend on the sign of n . The resulting spectrum is symmetric [62] and does not show odd-order sidebands. If, however,

a dc field is present, the sideband spectrum gets asymmetric and also odd-order sidebands are allowed. For an increasing amplitude of the ac field, the number of populated sidebands grows.

In analogy to the process described above, stimulated emission involving a distinct number of rf photons takes place if the coupling laser is not scanned, but instead locked resonantly with respect to the Stark-shifted Rydberg state. Due to the fixed phase relationship between the different sidebands (see Eq. 7.12) this leads to a modulation of the excitation light which acquires sidebands at $\pm n\omega$.

The validity of a Floquet approach as presented above was determined in Ref. [62] for $E_{dc} = 0$ to be limited to cases, where

$$\left| \frac{\Omega_c J_0(\alpha E_{ac}^2 / (8\hbar\omega))}{2\omega} \right| \ll 1. \quad (7.13)$$

Since the Bessel function is restricted to values smaller than one, this implies that the dynamics of the rf field must be much faster than the atomic evolution, determined by the Rabi frequency Ω_c . In the opposite limit, where the evolution of the atomic system is faster than the rf modulation, the system can follow adiabatically and no Floquet states can develop. It should be noted that in both cases a modulation of the excitation light is expected. In addition to the condition given in Eq. 7.13, the development of Floquet states requires a coherence time $1/\Gamma_{ryd}$ of the Rydberg state which is longer than the modulation period [62]. This requirement which can be expressed as

$$\Gamma_{ryd} \ll \omega \quad (7.14)$$

implies that the system has to interact with the rf field coherently for several modulation periods in order for the Floquet states to develop. In frequency space, the same condition implies that the line width of the states is sufficiently small so that the individual states do not overlap. The experimental results presented in the following were obtained in a regime where both above-mentioned requirements are met. While no dc field was applied, a small dc component (< 0.5 V/cm) was encountered due to local electric fields inside the fibers. The presented theoretical treatment proved to describe this situation adequately.

7.2 Electrical Addressing of Fiber Segments

The field plates integrated into the e-chamber detailed in Sec. 3.3 allow for the application of electric fields along a $60\text{ }\mu\text{m}$ kagome fiber and a $60\text{ }\mu\text{m}$ capillary. Due to the arrangement of the five individually contacted plates, the Stark effect can be employed to shift the Rydberg state in selected segments out of resonance. For large enough electric fields, the addressed segments cause a distinct spectroscopic signal which is well separated from the unshifted Rydberg line. By addressing different fiber segments, it is therefore possible to gain a spatial resolution of the probe spectra.

Fundamental Aspects

While dc electric fields have been employed to tune Rydberg resonances in thermal vapors [52, 75, 76], this approach requires field plates located inside the excitation volume to circumvent

charge screening effects [25]. The latter arise due to the unavoidable presence of charges in the system (e.g. caused by excited state collisions) which effectively screen dc fields. However, charge screening can be circumvented if an ac field is used and the field direction is switched faster than the charges can follow [51]. The charge relaxation time can be roughly estimated by considering the time a positively charged cesium atom needs to cross the excitation cross section for a given electric field. For a fiber diameter of 60 μm and electric fields on the order of 5 V/cm, this estimate leads to a required modulation frequency in the lower MHz regime. As a consequence, the electric field was modulated sinusoidal at a frequency of typically 500 MHz in the measurements described in the following. At this frequency and the typical field amplitudes employed in the experiment, the population of the Floquet states discussed in Sec. 7.1 is small. The main effect of the electric field is therefore a Stark shift of the carrier state.

This shift was used in the measurements presented in the following to address individual segments along the fibers. Rf-induced sidebands occurring at sufficiently large modulation amplitudes for a given modulation frequency are subject of Sec. 7.3. For all measurements presented in the following, the Rydberg state $30P_{3/2}$ was employed. While the polarizability of this state depends on the absolute value of the magnetic quantum number m_J (see Eq. 2.6), only $|m_J| = 1/2$ states are coupled to the $7S_{1/2}$ state for π -polarized excitation light. As a consequence, the polarizability of the $m_J = 1/2$ state $\alpha_{30P_{1/2}} = 26.93 \text{ MHz}/(\text{Vcm}^{-1})^2$ [35] was used to estimate the applied electric fields. In this context, it is important to note that the employed hollow-core fibers are not intrinsically polarization maintaining. However, since no splitting of the magnetic sublevels could be observed for the kagome fiber, it was concluded that the fiber can be regarded as polarization maintaining for short fiber lengths. This assumption could not be confirmed for the capillary. The emerging error in the estimated field strength is however small, since the polarizability of the $|m_J| = 3/2$ states $\alpha_{30P_{3/2}} = 22.21 \text{ MHz}/(\text{Vcm}^{-1})^2$ [35] does not deviate significantly from $\alpha_{30P_{1/2}}$.

Addressing

A schematic sketch of the field plate configuration is provided in Fig. 7.2. As discussed in Sec. 3.3, the plates generate an electric field perpendicular to the fibers if a potential with respect to the fiber holder (which acts as electrical ground) is applied. To simplify the theoretical treatment of the system, all laser beams are polarized linearly and parallel to the electric field. The modulation amplitudes given in the following have to be interpreted as

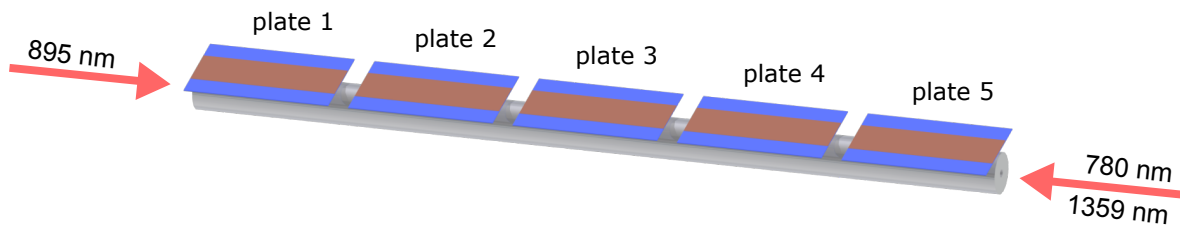


Figure 7.2: Schematic sketch of the field plate configuration. For reasons of clarity, only one of the two fibers is shown. Each plate consists of a glass substrate on which an electrically contacted silver stripe is evaporated (see Sec. 3.3). The fiber mount which holds the fibers is made of copper and acts as electrical ground plane.

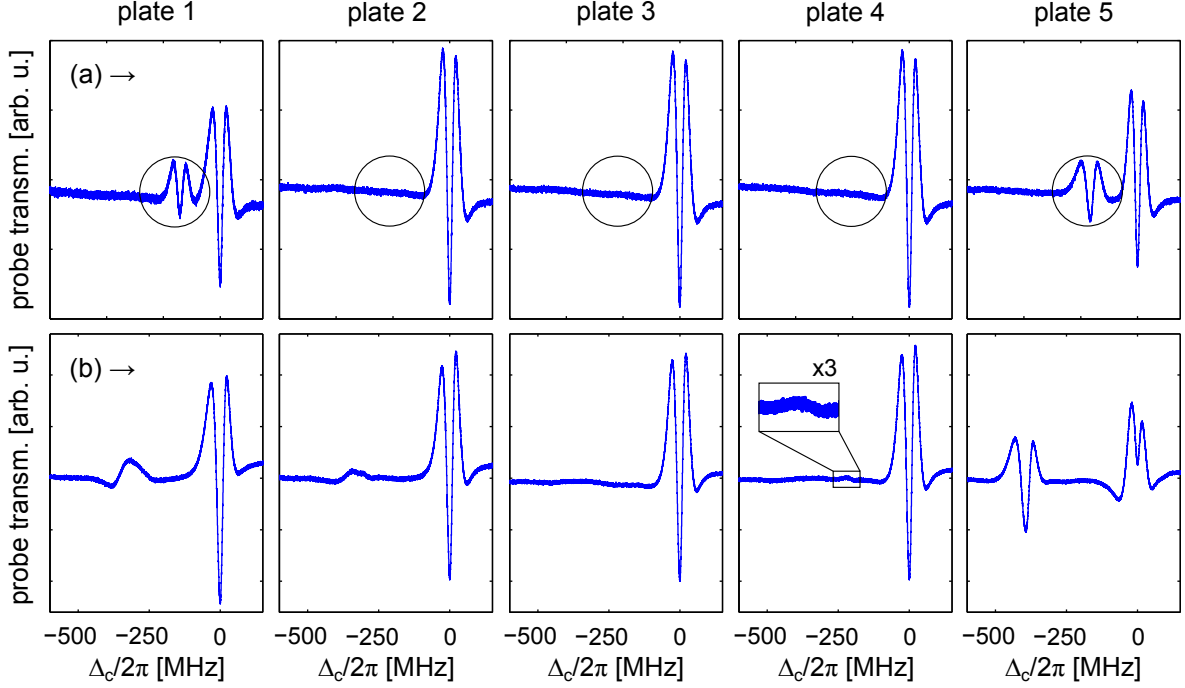


Figure 7.3: Probe spectra obtained in the 60 μm kagome fiber for the Rydberg state $30P_{3/2}$ and a modulation frequency of 500 MHz. Only one plate was modulated for each spectrum (indicated as defined in Fig. 7.2). (a) Spectra (averaged between 200 and 500 times) obtained after the fiber was exposed for thirteen days to cesium ($OD_{\text{chamber}} = 3.8$, $OD_{\text{kagome}} = 0.4$). The field amplitude of the ac field (estimated from the encountered shifts) was between 4.6 V/cm and 5 V/cm for a rf amplitude of 141 mV. The shifted signal (or the expected position of the latter) is marked by a black circle. (b) Spectra (averaged 200 times) obtained for high optical densities after the fiber was exposed almost two months to cesium ($OD_{\text{chamber}} = 21.6$, $OD_{\text{kagome}} = 8.2$). The rf amplitude was $U_{\text{rf}} = 225$ mV and the estimated ac field amplitude (below the fifth plate) $E_{\text{ac}} = 7.6$ V/cm.

the output voltages of the employed rf generator. Due to the transmission properties of the coaxial transmission lines (see Sec. 3.3), these voltages do not correspond to the voltages applied to the field plates. As a consequence, also the electric field amplitudes estimated from the encountered Stark shifts are given.

Figure 7.3a shows five spectra (see Ch. 4) obtained in the 60 μm kagome fiber for the modulation of a single plate at 500 MHz and a rf amplitude of $U_{\text{rf}} = 141$ mV. The modulated plate is indicated as defined in Fig. 7.2. All shown spectra were taken after the fiber was exposed for thirteen days to cesium at reservoir and chamber temperatures of $T_{\text{res}} = 33^\circ\text{C}$ and $T_{\text{ch}} = 84^\circ\text{C}$ respectively. For the two outermost plates two distinct three-photon signals are clearly visible. While the resonant signal ($\Delta_c = 0$) corresponds to all unmodulated parts of the fiber, the red-shifted signal is caused by atoms below the modulated segment. The fact that no shifted signal is present for the inner three plates can be attributed to the slow diffusion process of cesium atoms into the fiber (see Sec. 5.2) and is consistent with the measured optical densities ($OD_{\text{chamber}} = 3.8$, $OD_{\text{kagome}} = 0.4$). From the shift of the signals, the amplitude of the ac electric field can be estimated to be $E_{\text{ac}} = 4.6$ V/cm and $E_{\text{ac}} = 5$ V/cm below the first and the fifth plate respectively (see Sec. 7.1). Due to the relatively small optical density during the measurements, the probe beam was not significantly attenuated over the length of the fiber which is reflected in the similarity of the outer spectra

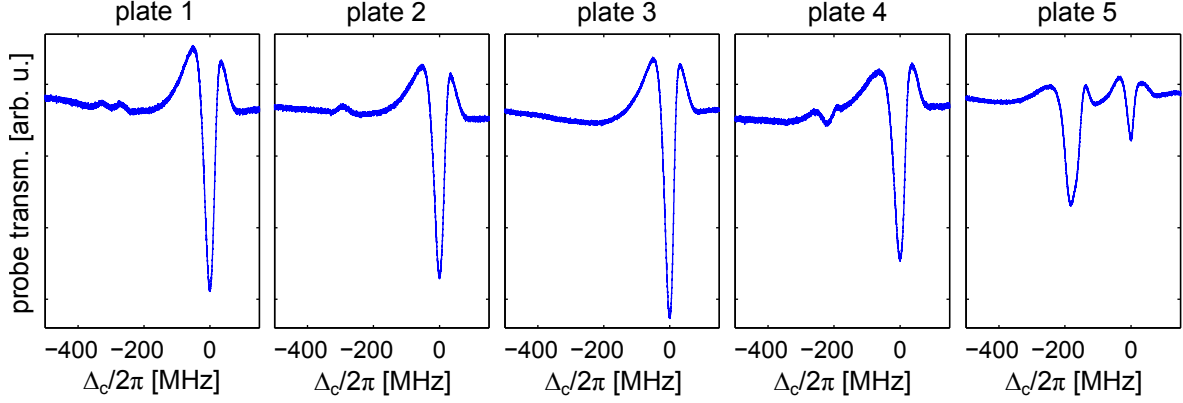


Figure 7.4: Probe spectra (averaged 500 times) obtained in the 60 μm capillary ($OD_{\text{chamber}} = 18.5$, $OD_{\text{capillary}} = 6.2$) for the Rydberg state $30P_{3/2}$. For each spectrum, one field plate was modulated at 500 MHz and a rf amplitude of $U_{\text{rf}} = 225$ mV for the first four plates and $U_{\text{rf}} = 141$ mV for the fifth plate. The estimated field amplitudes are $E_{\text{ac}} = \{6.7, 6.6, 5.7, 5.2\}$ V/cm for the first and last two field plates respectively.

in Fig. 7.3a. A comparison of the spectra with a typical three-photon signal obtained in the reference cell (see Fig. 4.4) reveals a slight lineshape deformation which might be attributed to local electric fields inside the fiber (see Ch. 6).

Since no signal below the inner field plates of the fiber could be observed for more than one month, the reservoir temperature was increased. Fig. 7.3b shows probe spectra obtained almost two months after the cesium reservoir was broken at optical densities of $OD_{\text{chamber}} = 21.6$ and $OD_{\text{kagome}} = 8.2$ in chamber and fiber respectively. The spectra still do not show a signal below the middle plate which is consistent with the measured optical densities, suggesting that the diffusion process still did not reach equilibrium. For the other two inner plates however, a small signal is visible. In contrast to the measurements taken at low optical densities, the spectra clearly reflect the attenuation of the probe beam. While the high probe power on the one side of the fiber caused a Gaussian like transmission lineshape (see Sec. 4.4), the attenuated probe power on the other side of the fiber caused a typical three-photon signal showing enhanced absorption on resonance. The qualitative change of the signal over the length of the fiber is particularly visible in the spectrum corresponding to the fifth plate.

Fig. 7.4 shows spectra measured in the modulated 60 μm capillary after it was exposed for one and a half months to cesium. The optical densities were determined to be $OD_{\text{chamber}} = 18.5$ and $OD_{\text{capillary}} = 6.2$ for chamber and fiber respectively. Similar to the kagome fiber, a shifted signal is visible for the four outer field plates. While the encountered shifts for a given rf power were slightly larger than in the case of the kagome fiber, the difference is on the few percent level. It is remarkable that the signal corresponding to the fifth fiber segment is by far the largest one. However, a quantitative prediction of the cesium densities corresponding to the spectroscopic signals is difficult due to the qualitative change of the signal along the fiber. Additionally, the attenuation of the laser beams due to the guiding properties of the capillary are unknown and local electric fields might have significant influence on the signal heights. With respect to the latter point, it is worth to note that the asymmetry present in all of the five spectra seems to originate mainly from the end of the fiber where the strong 780 nm beam is coupled in (see right spectrum in Fig. 7.4). While this observation does not allow

for in-depth conclusions, it might be explainable by charge productions during light-induced atomic desorption processes [77].

The presented results suggest that the employed design is well suited to gain a spatial resolution of the spectroscopic signal along a hollow-core fiber. It can therefore be employed to study the diffusion of atoms into hollow-core fibers in a much more detailed way than it is possible with plain absorption measurements (see Sec. 5.2). The results also suggest that diffusion measurements should be carried out at low optical densities to ensure an insignificant attenuation of the probe beam. To avoid lineshape deformations as encountered at high chamber temperatures (see Ch. 6), it is furthermore advantageous to work at low temperatures. A significant drawback of such conditions is however, that the diffusion process is expected to last much longer than in the case studied in Sec. 5.2, where a filling time of three weeks was estimated. For a systematic study, it is therefore highly beneficial to employ much shorter fiber lengths.

Performance of the Experimental Design

In the following, the performance of the employed experimental setup is briefly discussed. As described in Sec. 3.3, the individual field plates are connected with self-built coaxial cables to the feedthroughs. While the coaxial cables have an impedance of approximately $28\ \Omega$, the feedthroughs have an impedance of $50\ \Omega$ and the connections to the feedthroughs constitute short segments on which the impedance is not well defined. As a consequence, standing wave effects are expected. To determine if the latter limit the transmission of power to the field plates, the Stark shift of the signal was measured as a function of the rf voltage U_{rf} for the Rydberg state $30P_{3/2}$. Figure 7.5a shows the result for one of the field plates and a modulation frequency of 500 MHz. Due to the small geometry of the design, shifts of up to 1 GHz were achieved for rf voltages below 400 mV and a polarizability of $\alpha = 26.93\ \text{MHz}/(\text{Vcm}^{-1})^2$ [35]. By fitting a curve of the form $-1/4\alpha(\text{const} \cdot U_{\text{rf}})^2$ to the data (see Sec. 7.1), the electric field

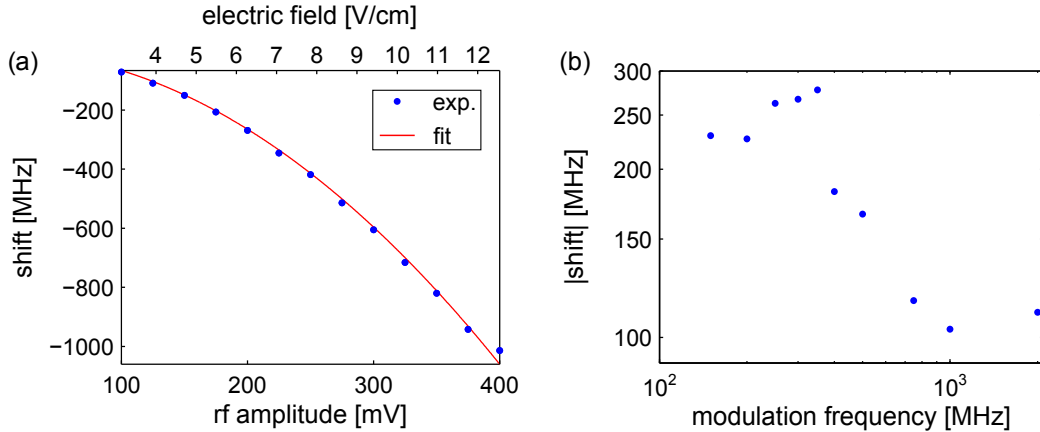


Figure 7.5: (a) Observed Stark shift for the $30P_{3/2}$ Rydberg state and the modulation of a single plate at 500 MHz at different rf voltages U_{rf} . By fitting a curve of the form $-1/4\alpha(\text{const} \cdot U_{\text{rf}})^2$, the electric field amplitude was determined (see upper axis) and the transfer efficiency of the rf input voltage was estimated to be 70 %. (b) Frequency behavior of the coaxial transmission line for modulation frequencies up to 2 GHz and a rf amplitude of $U_{\text{rf}} = 150\ \text{mV}$. Given is the absolute value of the encountered line shift of the $30P_{3/2}$ Rydberg state.

amplitude corresponding to the rf voltage was extracted (upper axis of Fig. 7.5a). Based on the distance between the field plates and the fiber holder and the assumption, that every field plate essentially constitutes an open end of the coaxial transmission line (see Sec. 3.3), the transfer efficiency of the input rf voltage U_{rf} was estimated to be approximately 70 % at a frequency of 500 MHz. While the quadratic fit in Fig. 7.5a fits well to the experimental data, charge screening effects depend on the amplitude of the applied field. For small modulation frequencies at which screening effects get relevant, deviations from the theoretical expected shift are therefore expected and could qualitatively be observed in the experiment.

To evaluate the frequency behavior of the transmission line, and especially if the modulation bandwidth is limited to the MHz regime, spectra were taken for different modulation frequencies at a constant rf voltage. Figure 7.5b shows the absolute value of the encountered shifts of the Rydberg line for modulation frequencies up to 2 GHz (which was the limit of the employed rf generator). While a frequency dependence of the Stark shift is clearly observable, the decrease of the shift at high frequencies does not constitute a limiting factor in terms of the bandwidth. However, the frequency behavior of the transmission efficiency is undesirable and might well be improved by an impedance matching circuit installed outside of the vacuum chamber.

7.3 Rf-induced Sidebands of the Rydberg State

While the last section focused on the electric field induced shift of the Rydberg line, the theoretical model discussed in Sec. 7.1 also predicts the formation of sidebands under the action of an ac field. Such sidebands were observed in the experiment and found to be well described by the employed theory. In the following, experimental results obtained in the 60 μm kagome fiber are presented and the influence of the modulation frequency and modulation amplitude is discussed. Subsequently, the experimental findings are compared to the theoretical model. In all measurements presented here, the Rydberg state was $30P_{3/2}$,

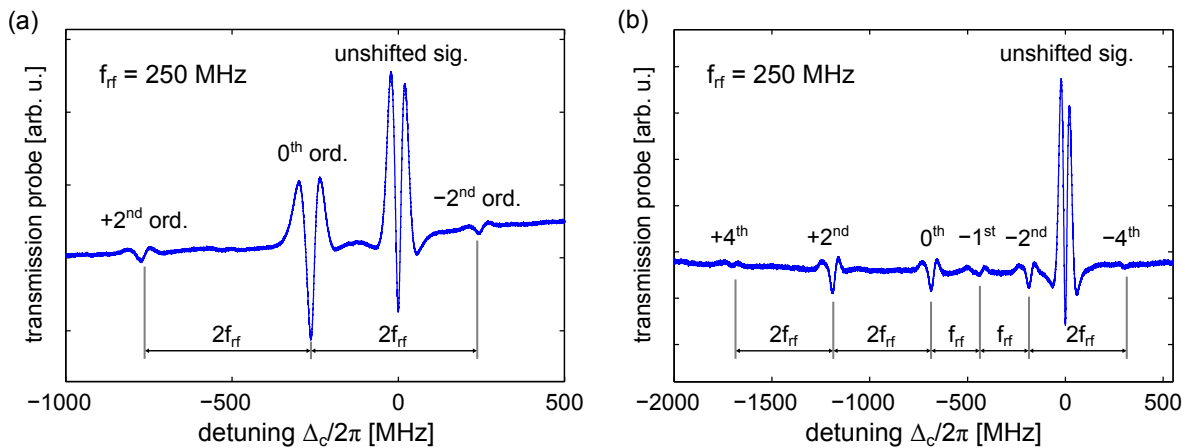


Figure 7.6: Probe spectra obtained (averaged 500 times) at a rf modulation frequency of 250 MHz and modulation amplitudes U_{rf} of 150 mV and 250 mV in (a) and (b) respectively. Only one field plate (plate 5) was modulated. At higher modulation amplitudes, the number of populated sidebands increases. The existence of the minus first order sideband in (b) can be attributed to local electric dc fields inside the fiber (see Ch. 6).

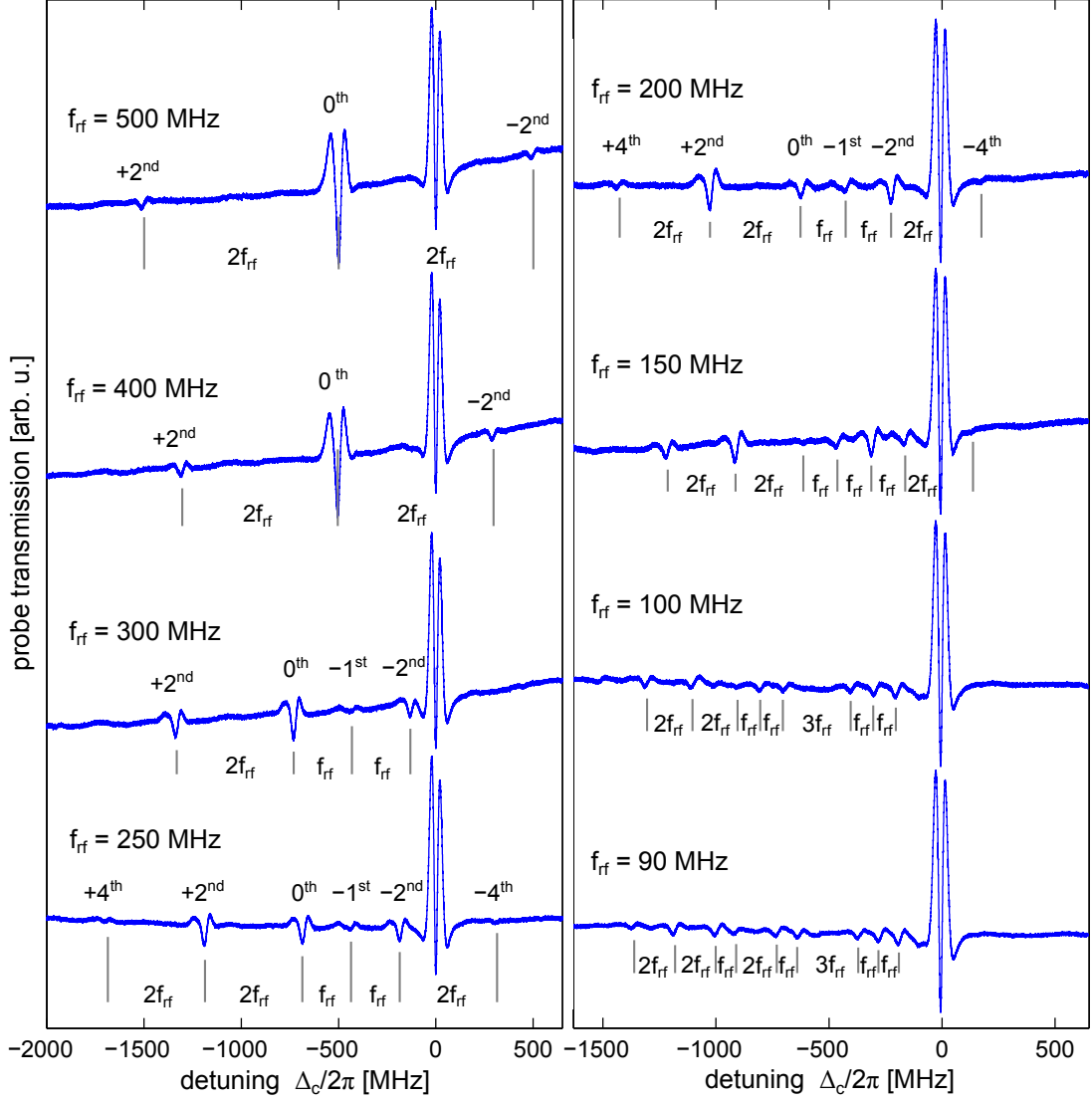


Figure 7.7: Frequency behavior of the observed sideband spectra (averaged 500 times) at a constant rf amplitude of $U_{\text{rf}} = 250$ mV. The modulation frequency is indicated in the spectra. Note that the position of the carrier state is slightly frequency dependent due to the transmission properties of the coaxial cable (see Sec. 7.2). With decreasing modulation frequency, the number of populated sidebands increases. This is consistent with the theoretical sideband amplitudes $|A_n|^2$ determined by Eq. 7.11.

only one plate (plate 5, see Sec. 7.2) was modulated and the optical density in the fiber was $OD_{\text{kagome}} = 4.4$.

Figure 7.6a shows a spectrum taken at a modulation frequency of $f_{\text{rf}} = 250$ MHz and a rf amplitude of $U_{\text{rf}} = 150$ mV. As in the spectra presented before (see Fig. 7.3), the biggest two signals correspond to the unshifted Rydberg line (respectively the unaddressed segments of the fiber) and the red-shifted carrier state (respectively the modulated part of the fiber). Additionally, two sidebands at $\pm 2f_{\text{rf}}$ with respect to the carrier state are clearly visible. Since no dc electric field was applied, the non-existence of the first order sidebands is expected. From the discussed theoretical model, it is expected that the number of populated sidebands increases with the modulation amplitude (see Fig. 7.1b). Qualitatively, this can be seen in

Fig. 7.6b, showing a spectrum taken at a rf frequency of $f_{\text{rf}} = 250$ MHz and a modulation amplitude of $U_{\text{rf}} = 250$ mV. Due to the increased ac field, the carrier state is shifted further to the red and more sidebands can be observed. Strikingly, not only fourth order sidebands appear in the spectrum, but also the minus first order is visible. As discussed in Sec. 7.1, odd-order sidebands as well as asymmetries in the sideband spectrum are induced by dc electric fields. Since no offset field was applied in the measurement, the observations must be attributed to a local electric field inside the fiber. While such a field was previously assumed (see Ref. [24] and Ch. 6), this finding constitutes an independent confirmation of its existence. It is interesting to note that the carrier state which is by far the most populated state at low modulation amplitudes, depopulates at higher modulation amplitudes. This can be clearly observed in the shown spectra and is a direct consequence of Eq. 7.11 which determines the amplitude of the sidebands.

To determine if the frequency behavior of the sideband spectra is adequately described by the employed theoretical model, spectra were taken at constant rf amplitude and various modulation frequencies. Fig. 7.7 shows the experimental results for $U_{\text{rf}} = 250$ mV and rf frequencies between 90 MHz and 500 MHz. It is clearly visible that the effect of the modulation frequency is complementary to that of the modulation amplitude. While a rich spectrum of sidebands is observable at low modulation frequencies, the number of populated sidebands decreases with increasing modulation frequency until the carrier state is by far the most populated state. The red-shift of the latter is slightly frequency dependent which can be attributed to the frequency behavior of the coaxial transmission line (see Sec. 7.2). As a consequence, a definite assignment of the carrier state in the shown spectra can not be given for modulation frequencies lower than 200 MHz. For the spectra taken at modulation frequencies between 200 MHz and 300 MHz, the position of the carrier state was estimated from the frequency dependent Stark shift at lower field amplitudes (see Fig. 7.5b) and confirmed by a comparison of the sideband amplitudes with theoretical predictions (see Sec. 7.1). From the shown spectra, the relative amplitude of the second order sidebands (averaged over the positive and negative order) was estimated to be approximately 5 % at a modulation frequency of 500 MHz and 29 % at a modulation frequency of 250 MHz.

In the following, the experimental results are compared to theoretical predictions based on the model discussed in Sec. 7.1. In this context, it is important to note that the dc field and the ac field were assumed to be parallel in the theoretical treatment. Due to the unknown nature of the local electric dc field in the fiber, this assumption is most probably not met in the experiment. However, the dc field is expected to be small in comparison to the applied ac fields, and the anisotropy of the polarizability of the employed $P_{3/2}$ Rydberg state is small. This can be seen by comparing the polarizabilities of the magnetic substates $|m_J| = 1/2$ and $|m_J| = 3/2$ which are $\alpha_{1/2} = 26.93 \text{ MHz}/(\text{Vcm}^{-1})^2$ and $\alpha_{3/2} = 22.21 \text{ MHz}/(\text{Vcm}^{-1})^2$ respectively [35]. The simplified theoretical treatment therefore constitutes a good approximation of the experimental situation. The amplitude of the experimentally observed sidebands was determined by fitting a quadratic function to the maxima and minima of the corresponding three-photon signal. To account for asymmetries, the amplitude was determined using the average of the two transmission maxima of each signal. The theoretically expected sideband amplitudes are given by the coefficients $|A_n|^2$ defined by Eq. 7.11. For a given modulation frequency, the only free parameters in these coefficients are the ac and dc electric field amplitudes. Accordingly, $|A_n|^2$ was fitted to the experimental data, treating E_{dc} and E_{ac}

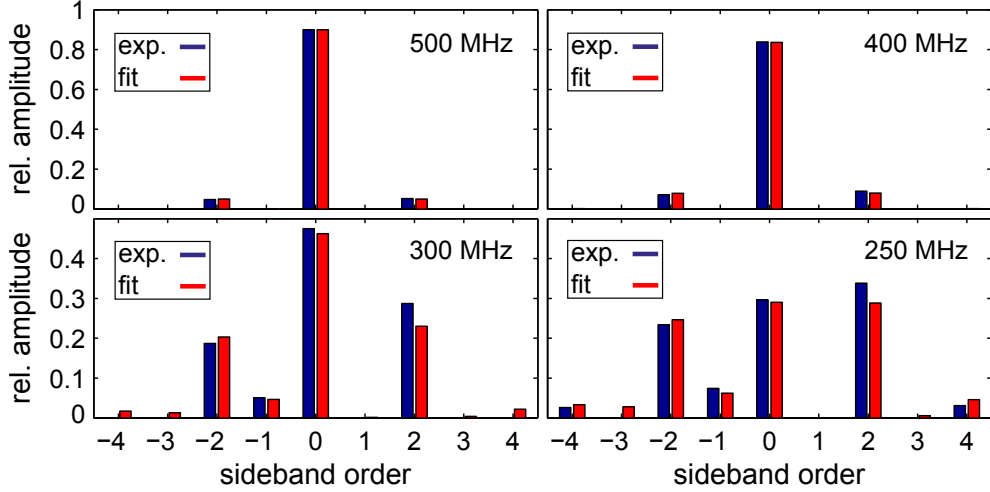


Figure 7.8: Relative amplitude of the sidebands at different modulation frequencies. The experimental results are shown together with the fitted theoretical amplitude $|A_n|^2$ (see Eq. 7.11). Both E_{ac} and E_{dc} were treated as free fit parameters and determined to be $E_{ac} = \{8.24 \pm 0.03, 8.36 \pm 0.08, 10.05 \pm 0.19, 10.20 \pm 0.16\}$ V/cm and $E_{dc} = \{0.03 \pm 0.22, 0.1 \pm 0.2, 0.41 \pm 0.1, 0.41 \pm 0.07\}$ V/cm at modulation frequencies of $\{500, 400, 300, 250\}$ MHz. The ac field amplitudes have to be compared with an estimation based on the Stark shift of the carrier state and the assumption $E_{dc} = 0$: $E_{ac} = \{8.58, 8.66, 10.43, 10.08\}$ V/cm. The fitted ac field amplitudes agree with these estimated amplitudes to a precision better than 4%.

as fit parameters. The experimental results are shown together with the fit in Fig. 7.8 for modulation frequencies between 250 MHz and 500 MHz. It can be seen that especially for high modulation frequencies, the theoretical model is in excellent agreement with the experimental data. To ensure that the fit provides realistic values for the electric fields, the ac field amplitude E_{ac} was estimated from the shift of the carrier state under the assumption that the dc field can be neglected. It was found that the fitted field amplitudes agree with the estimated amplitudes to a precision better than 4%. The fitted field amplitudes of the dc field E_{dc} are between (0.03 ± 0.22) V/cm at $f_{rf} = 500$ MHz and (0.41 ± 0.07) V/cm at $f_{rf} = 250$ MHz. These values suggest that the local electric field inside the fiber might depend on the modulation frequency. This could be explained by the influence of the applied ac fields on the charge distribution inside the fiber. Considering the good agreement between the theoretical and experimental sideband spectra, the employed theory seems to describe the experimental situation adequately.

With respect to potential applications, the achievable sideband amplitudes are of great interest. A particular simple expression for the latter can be given in the absence of a dc field. Under these conditions, the infinite sum in Eq. 7.11 reduces to a single term. For the second order sidebands (which are of particular interest), the amplitude is then given by

$$|A_2(y)|^2 = |J_1(y)|^2, \quad (7.15)$$

where the argument of the Bessel function is defined by $y = \alpha E_{ac}^2 / (8\hbar\omega)$ and ω is the angular frequency of modulation ($\omega = 2\pi f_{rf}$). While the assumption $E_{dc} = 0$ was not met in the experiment, it was found that the qualitative behavior of the sidebands is still well described by Eq. 7.15 for the small dc fields which were present in the experiment and the parameter range examined. Figure 7.9 shows a plot of $|A_2(y)|^2$ together with experimental data obtained

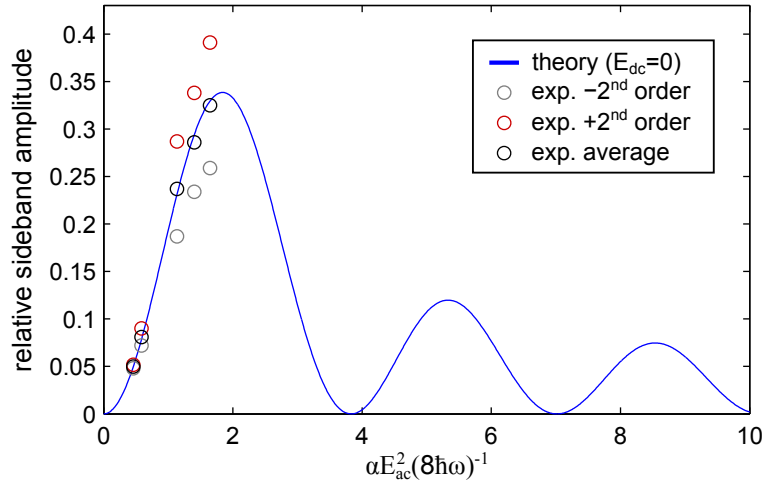


Figure 7.9: For the case of a vanishing dc field, the sideband amplitude only depends on the parameter $y = \alpha E_{ac}^2 / (8\hbar\omega)$, where ω is the (angular) modulation frequency. Shown is the theoretical amplitude of the second order sidebands for $E_{dc} = 0$ together with experimental data (see Fig. 7.7). For the latter, y was determined by fitting the full sideband spectrum (see Fig. 7.8). Fitting errors are within the marker size. The asymmetry of the plus and minus order sidebands present in the experimental data is due to a small dc field. For the examined parameter range, the average sideband amplitude can be seen to match qualitatively to the case where $E_{dc} = 0$. For $E_{dc} = 0$, a maximum relative sideband amplitude of approximately 33.9% at $y \approx 1.842$ is theoretically predicted.

from the spectra shown in Fig. 7.7. For the experimental results, the ac field amplitude E_{ac} was determined by fitting the full theoretical model to the sideband spectrum (see Fig. 7.8). In contrast to the predictions of Eq. 7.15, an asymmetry of the positive and negative order sidebands is visible due to the dc field present in the experiment. The average amplitude, however, is well approximated by Eq. 7.15. From the theory curve, a maximum relative sideband amplitude of approximately 33.9% at $y \approx 1.842$ can be extracted. Within the limits of validity of the employed theoretical model (see Sec. 7.1), this optimal sideband height can be achieved for all modulation frequencies if an according ac field amplitude is chosen. As reflected in the shown experimental data, higher amplitudes can be achieved in the presence of a dc field which induces an asymmetry of the plus and minus order sidebands.

8 Conclusion and Outlook

While the study of Rydberg physics in hollow-core fibers is in its early stages, this field of research is promising. However, the understanding of the observed line shifts and broadenings (see Sec. 6 and Ref. [23, 24]) is crucial for the further development of the system. While in this work 60 μm hollow-core fibers have been employed, it is of fundamental interest if Rydberg excitation can be achieved in few-micrometer core diameters. Rydberg-Rydberg interactions over distances on the order of the fiber diameter would then correspond to a sufficiently large energy scale to induce optical nonlinearities. As a consequence, the system might allow for the generation of non-classical light in a thermal vapor.

In the scope of this thesis, rf-dressed Rydberg states inside of hollow-core fibers have been investigated (see Ch. 7). The results obtained in this context (see Sec. 7.3) suggest that the design of the built apparatus (see Sec. 3.3) is well suited for its purpose. Due to the small geometry of the fiber-field plate assembly and the high polarizability of Rydberg atoms, the setup allows for an energy modulation of Rydberg states and with this a modulation of the excitation light at low rf powers. Rf-induced sidebands separated up to 1 GHz from the carrier Rydberg state could be observed at rf powers and amplitudes of 1 dBm and ~ 10 V/cm respectively. A relevant improvement of the design could be achieved by replacing the field plates by conductive wires directly integrated into the fiber [78] or by the evaporation of the field plates onto the fiber cladding. Such a design would allow for even lower modulation powers and essentially constitute an ultra-low power Rydberg-based fiber modulator.

Not only with respect to possible future applications it is desirable to omit a bulky vacuum setup and close the employed hollow-core fibers vacuum tight by splicing standard step-index fibers to the open ends [15]. A filling of these fibers with alkali vapor might then be achieved through microscopic holes through the side of the fiber cladding [79, 80] which can be sealed after an appropriate amount of time determined by the diffusion process of the vapor into the fiber (see Ch. 5). Such an assembly would both make the experimental setup much more compact and constitute a major step towards miniaturized integrated devices.

The employed three-photon excitation of the Rydberg state (see Ch. 4) is advantageous in the sense that only infrared wavelengths are used, for which high power diode lasers and amplifiers are commercially available. Moreover, a narrow spectroscopic feature (~ 10 MHz) can be achieved on resonance. As a consequence of the resonant three-photon transition however, this feature is of absorptive nature. For quantum-optics experiments, it is therefore beneficial to change to a two-photon excitation scheme in which enhanced transmission on resonance and slow light can be achieved due to electromagnetically induced transparency [81].

The results of this thesis and of previous work [23, 24] suggest that Rydberg atoms inside hollow-core fibers are a promising system in two ways. On the one hand, the reduction of the employed fiber core diameters could allow for the investigation of quasi-one-dimensional Rydberg systems. On the other hand, the results suggest that room temperature Rydberg-based

applications such as ultra-low power fiber modulators or miniaturized microwave sensors [13, 24] are technically feasible and within reach in the near future.

Appendix

A Physical and Atomic Properties of Cs

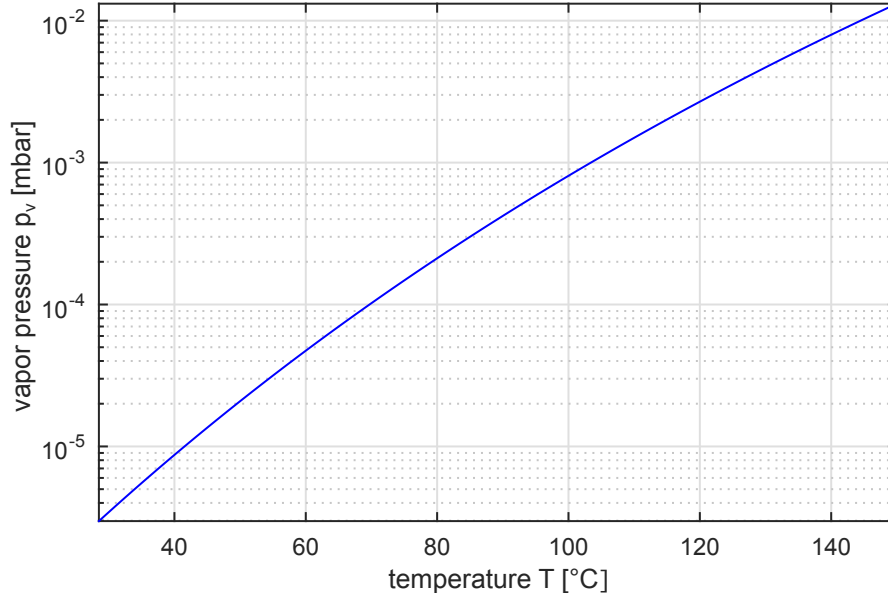


Figure A.1: Vapor pressure of liquid cesium according to Eq. 2.1.

property	value
number of protons Z	55
nuclear spin I	$7/2$
atomic mass m	$2.20694657(11) \times 10^{-25} \text{ kg}$
melting point T_m	28.5°C
boiling point T_b	671°C
vapor pressure P_v at 25°C	$1.983 \times 10^{-4} \text{ Pa}$

Table A.1: Selected physical properties of ^{133}Cs [31].

transition	$\langle J \ e\mathbf{r} \ J' \rangle$	reference
$6S_{1/2} \rightarrow 6P_{1/2}$	$2.7020(50) \times 10^{-29} \text{ Cm}$	[31]
$6P_{1/2} \rightarrow 7S_{1/2}$	$(3.590 / \sqrt{2}) \times 10^{-29} \text{ Cm}$	[82]
$7S_{1/2} \rightarrow nP_{3/2}$	$0.8165 \times 3.390 e a_0 (n - \delta)^{-3/2}$	[23]

Table A.2: Reduced dipole matrix elements for selected transitions in cesium. Note that a factor of $\sqrt{2}$ appears in the matrix element of the $6P_{1/2} \rightarrow 7S_{1/2}$ transition due to different conventions used. For the Rydberg transition, the matrix element was determined from the radial dipole matrix element given in Ref. [23]. e is the elementary charge, a_0 is the Bohr radius and δ is the quantum defect of the Rydberg state (see Sec. 2.2).

n	$7S_{1/2} \rightarrow nP_{1/2}$	$7S_{1/2} \rightarrow nP_{3/2}$
25	791.672	791.627
26	790.364	790.324
27	789.225	789.189
28	788.224	788.193
29	787.343	787.315
30	786.560	786.536
31	785.863	785.842
32	785.239	785.220
33	784.680	784.663
34	784.174	784.159
35	783.717	783.703
36	783.303	783.290
37	782.925	782.913
38	782.579	782.569
39	782.263	782.254
40	781.986	781.964
41	781.706	781.698
42	781.461	781.453
43	781.233	781.226
44	781.022	781.016
45	780.826	780.820
46	780.645	780.639
47	780.476	780.470
48	780.317	780.312
49	780.170	780.165
50	780.032	780.027
51	779.902	779.898
52	779.781	779.777
53	779.667	779.663
54	779.560	779.556
55	779.458	779.455
56	779.363	779.360
57	779.273	779.270
58	779.188	779.185
59	779.108	779.105
60	779.031	779.029

Table A.3: Rydberg transition wavelengths (in nm) for the transition $7S_{1/2} \rightarrow nP$ for main quantum numbers n between 25 and 60 [23]. The transition wavelengths are given for both existing J states.

B Bibliography

- [1] N. Bohr, “I. On the constitution of atoms and molecules”, The London, Edinburgh, and Dublin Philosophical Magazine and Journal of Science **26**, 1–25 (1913).
- [2] H. Marion, F. P. Dos Santos, M. Abgrall, S. Zhang, Y. Sortais, S. Bize, I. Maksimovic, D. Calonico, J. Grünert, C. Mandache, et al., “Search for variations of fundamental constants using atomic fountain clocks”, Physical Review Letters **90**, 150801 (2003).
- [3] C. Monroe, “Quantum information processing with atoms and photons”, Nature **416**, 238–246 (2002).
- [4] N. Hinkley, J. Sherman, N. Phillips, M. Schioppo, N. Lemke, K. Beloy, M. Pizzocaro, C. Oates, and A. Ludlow, “An atomic clock with 10^{-18} instability”, Science **341**, 1215–1218 (2013).
- [5] T. F. Gallagher, *Rydberg atoms*, Vol. 3 (Cambridge University Press, 2005).
- [6] R. Löw, H. Weimer, J. Nipper, J. B. Balewski, B. Butscher, H. P. Büchler, and T. Pfau, “An experimental and theoretical guide to strongly interacting Rydberg gases”, Journal of Physics B: Atomic, Molecular and Optical Physics **45**, 113001 (2012).
- [7] O. Firstenberg, T. Peyronel, Q.-Y. Liang, A. V. Gorshkov, M. D. Lukin, and V. Vuletić, “Attractive photons in a quantum nonlinear medium”, Nature **502**, 71–75 (2013).
- [8] Y. Dudin and A. Kuzmich, “Strongly interacting Rydberg excitations of a cold atomic gas”, Science **336**, 887–889 (2012).
- [9] L. Isenhower, E. Urban, X. Zhang, A. Gill, T. Henage, T. A. Johnson, T. Walker, and M. Saffman, “Demonstration of a neutral atom controlled-not quantum gate”, Physical Review Letters **104**, 010503 (2010).
- [10] H. Gorniaczyk, C. Tresp, J. Schmidt, H. Fedder, and S. Hofferberth, “Single-photon transistor mediated by interstate Rydberg interactions”, Physical Review Letters **113**, 053601 (2014).
- [11] H. Kübler, J. Shaffer, T. Baluktsian, R. Löw, and T. Pfau, “Coherent excitation of Rydberg atoms in micrometre-sized atomic vapour cells”, Nature Photonics **4**, 112–116 (2010).
- [12] B. Huber, T. Baluktsian, M. Schlagmüller, A. Kölle, H. Kübler, R. Löw, and T. Pfau, “GHz Rabi flopping to Rydberg states in hot atomic vapor cells”, Physical Review Letters **107**, 243001 (2011).
- [13] J. A. Sedlacek, A. Schwettmann, H. Kübler, R. Löw, T. Pfau, and J. P. Shaffer, “Microwave electrometry with Rydberg atoms in a vapour cell using bright atomic resonances”, Nature Physics **8**, 819–824 (2012).
- [14] P. Russell, “Photonic crystal fibers”, Science **299**, 358–362 (2003).

-
- [15] F. Benabid, F. Couny, J. Knight, T. Birks, and P. S. J. Russell, “Compact, stable and efficient all-fibre gas cells using hollow-core photonic crystal fibres”, *Nature* **434**, 488–491 (2005).
 - [16] A. Lurie, F. N. Baynes, J. D. Anstie, P. S. Light, F. Benabid, T. M. Stace, and A. N. Luiten, “High-performance iodine fiber frequency standard”, *Optics Letters* **36**, 4776–4778 (2011).
 - [17] M. Bajcsy, S. Hofferberth, V. Balic, T. Peyronel, M. Hafezi, A. S. Zibrov, V. Vuletic, and M. D. Lukin, “Efficient all-optical switching using slow light within a hollow fiber”, *Physical Review Letters* **102**, 203902 (2009).
 - [18] S. Okaba, T. Takano, F. Benabid, T. Bradley, L. Vincetti, Z. Maizelis, V. Yampol’Ski, F. Nori, and H. Katori, “Lamb-Dicke spectroscopy of atoms in a hollow-core photonic crystal fibre”, *Nature Communications* **5** (2014).
 - [19] P. Londero, V. Venkataraman, A. R. Bhagwat, A. D. Slepikov, and A. L. Gaeta, “Ultralow-power four-wave mixing with Rb in a hollow-core photonic band-gap fiber”, *Physical Review Letters* **103**, 043602 (2009).
 - [20] S. Ghosh, A. R. Bhagwat, C. K. Renshaw, S. Goh, A. L. Gaeta, and B. J. Kirby, “Low-light-level optical interactions with rubidium vapor in a photonic band-gap fiber”, *Physical Review Letters* **97**, 023603 (2006).
 - [21] P. Light, F. Benabid, F. Couny, M. Maric, and A. Luiten, “Electromagnetically induced transparency in Rb-filled coated hollow-core photonic crystal fiber”, *Optics Letters* **32**, 1323–1325 (2007).
 - [22] M. Sprague, P. Michelberger, T. Champion, D. England, J. Nunn, X.-M. Jin, W. Kolthammer, A. Abdolvand, P. S. J. Russell, and I. Walmsley, “Broadband single-photon-level memory in a hollow-core photonic crystal fibre”, *Nature Photonics* **8**, 287–291 (2014).
 - [23] K. Kleinbach, *Rydberg spectroscopy in hollow core fibers*, Master thesis, Universität Stuttgart, 5. Physikalisches Institut, 2014.
 - [24] G. Epple, K. Kleinbach, T. Euser, N. Joly, T. Pfau, P. S. J. Russell, and R. Löw, “Rydberg atoms in hollow-core photonic crystal fibres”, *Nature Communications* **5** (2014).
 - [25] A. Mohapatra, T. Jackson, and C. Adams, “Coherent optical detection of highly excited Rydberg states using electromagnetically induced transparency”, *Physical Review Letters* **98**, 113003 (2007).
 - [26] A. K. Mohapatra, M. G. Bason, B. Butscher, K. J. Weatherill, and C. S. Adams, “A giant electro-optic effect using polarizable dark states”, *Nature Physics* **4**, 890–894 (2008).
 - [27] Y. Zhang, M. Ciocca, L.-W. He, C. Burkhardt, and J. Leventhal, “Measurement of atomic polarizabilities using Floquet spectroscopy”, *Physical Review A* **50**, 1101 (1994).
 - [28] J. Baugh, M. Ciocca, D. Edmonds, P. Nellesen, C. Burkhardt, and J. Leventhal, “Polarizability of a hydrogenic state”, *Physical Review A* **54**, R4641 (1996).
 - [29] C. van Ditzhuijzen, A. Tauschinsky, and H. v. L. Van Den Heuvel, “Observation of Stückelberg oscillations in dipole-dipole interactions”, *Physical Review A* **80**, 063407 (2009).

- [30] M. G. Bason, M. Tanasittikosol, A. Sargsyan, A. Mohapatra, D. Sarkisyan, R. Potvliege, and C. Adams, “Enhanced electric field sensitivity of rf-dressed Rydberg dark states”, *New Journal of Physics* **12**, 065015 (2010).
- [31] D. A. Steck, *Cesium D line data*, available online at <http://steck.us/alkalidata> (revision 2.1.4, 23 December 2010).
- [32] C.-J. Lorenzen and K. Niemax, “Precise quantum defects of ns, np and nd levels in Cs I”, *Zeitschrift für Physik A Atoms and Nuclei* **315**, 127–133 (1984).
- [33] A. Khadjavi, A. Lurio, and W. Happer, “Stark effect in the excited states of Rb, Cs, Cd, and Hg”, *Physical Review* **167**, 128 (1968).
- [34] R. W. Schmieder, A. Lurio, and W. Happer, “Quadratic Stark effect in the $^2P_{3/2}$ states of the alkali atoms”, *Physical Review A* **3**, 1209 (1971).
- [35] S. Gu, S. Gong, B. Liu, J. Wang, Z. Dai, T. Lei, and B. Li, “Experimental study of caesium atom Rydberg state polarizabilities by Doppler-free resonantly enhanced two-photon technique”, *Journal of Physics B: Atomic, Molecular and Optical Physics* **30**, 467 (1997).
- [36] M. O. Scully, *Quantum optics* (Cambridge University Press, 1997).
- [37] D. A. Steck, *Quantum and atom optics*, available online at <http://steck.us/teaching> (2006).
- [38] J. D. Pritchard, *Cooperative optical non-linearity in a blockaded Rydberg ensemble* (Springer Science & Business Media, 2012).
- [39] W. Demtröder, “Laserspektroskopie 1”, Springer-Verlag Berlin Heidelberg (2011).
- [40] J. Sagle, R. K. Namiotka und J. Huennekens, “Measurement and modelling of intensity dependent absorption and transit relaxation on the cesium D₁ line”, *J. Phys. B.* **29**, S. 2629–2643 (1996).
- [41] E. Marcatili and R. Schmeltzer, “Hollow metallic and dielectric waveguides for long distance optical transmission and lasers”, *Bell System Technical Journal* **43**, 1783–1809 (1964).
- [42] F. K. Kneubühl and M. W. Sigrist, *Laser* (Springer-Verlag, 2008).
- [43] R. K. Nubling and J. A. Harrington, “Launch conditions and mode coupling in hollow-glass waveguides”, *Optical Engineering* **37**, 2454–2458 (1998).
- [44] R. Cregan, B. Mangan, J. Knight, T. Birks, P. S. J. Russell, P. Roberts, and D. Allan, “Single-mode photonic band gap guidance of light in air”, *Science* **285**, 1537–1539 (1999).
- [45] F. Benabid and P. Roberts, “Linear and nonlinear optical properties of hollow core photonic crystal fiber”, *Journal of Modern Optics* **58**, 87–124 (2011).
- [46] G. Pearce, G. Wiederhecker, C. Poulton, S. Burger, and P. St J Russell, “Models for guidance in kagome-structured hollow-core photonic crystal fibres”, *Optics Express* **15**, 12680–12685 (2007).
- [47] P. Ilzhöfer, *Spektroskopie von thermischem Cäsium-Dampf in Hohlkernfasern*, Bachelor thesis, Universität Stuttgart, 5. Physikalisches Institut, 2012.

-
- [48] L. Bauer, *Sättigungsspektroskopie in Cäsium-gefüllten Glaskapillaren*, Diploma thesis, Universität Stuttgart, 5. Physikalisches Institut, 2012.
 - [49] J. M. Lamberti and N. T. Saunders, *Compatibility of cesium vapor with selected materials at temperatures to 1200 °F*, tech. rep. (National Aeronautics and Space Administration. Lewis Research Center, Cleveland, 1963).
 - [50] P. Wagner and S. R. Coriell, “On the high-temperature compatibility of cesium gas with some dielectrics”, *Review of Scientific Instruments* **30**, 937–938 (1959).
 - [51] R. Ritter, *Herstellung und Charakterisierung elektrisch adressierbarer Dampfzellen zur Rydbergspektroskopie*, Diploma thesis, Universität Stuttgart, 5. Physikalisches Institut, 2011.
 - [52] R. Daschner, R. Ritter, H. Kübler, N. Frühauf, E. Kurz, R. Löw, and T. Pfau, “Fabrication and characterization of an electrically contacted vapor cell”, *Optics Letters* **37**, 2271–2273 (2012).
 - [53] P. C. Hobbs, *Building electro-optical systems: making it all work* (Wiley, 2009).
 - [54] W. Demtröder, *Experimentalphysik 3: Atome, Moleküle und Festkörper*, Springer-Lehrbuch (Springer Berlin Heidelberg, Berlin, Heidelberg, 2010).
 - [55] C. Carr, M. Tanasittikosol, A. Sargsyan, D. Sarkisyan, C. S. Adams, and K. J. Weatherill, “Three-photon electromagnetically induced transparency using Rydberg states”, *Optics Letters* **37**, 3858–3860 (2012).
 - [56] S. Gilbert, R. Watts, and C. Wieman, “Hyperfine-structure measurement of the 7S state of cesium”, *Physical Review A* **27**, 581 (1983).
 - [57] O. Heavens, “Radiative transition probabilities of the lower excited states of the alkali metals”, *JOSA* **51**, 1058–1061 (1961).
 - [58] H. B. Michaelson, “The work function of the elements and its periodicity”, *Journal of Applied Physics* **48**, 4729–4733 (1977).
 - [59] T. Petelski, M. Fattori, G. Lamporesi, J. Stuhler, and G. Tino, “Doppler-free spectroscopy using magnetically induced dichroism of atomic vapor: a new scheme for laser frequency locking”, *The European Physical Journal D-Atomic, Molecular, Optical and Plasma Physics* **22**, 279–283 (2003).
 - [60] C. Carr, C. S. Adams, and K. J. Weatherill, “Polarization spectroscopy of an excited state transition”, *Optics Letters* **37**, 118–120 (2012).
 - [61] C. Carr, “Cooperative non-equilibrium dynamics in a thermal Rydberg ensemble”, PhD thesis (Durham University, 2013).
 - [62] M. Tanasittikosol, “Rydberg dark states in external fields”, PhD thesis (Durham University, 2011).
 - [63] J. Henningsen and J. Hald, “Dynamics of gas flow in hollow core photonic bandgap fibers”, *Applied Optics* **47**, 2790–2797 (2008).
 - [64] H. Babovsky, “On Knudsen flows within thin tubes”, *Journal of Statistical Physics* **44**, 865–878 (1986).
 - [65] I. Dicaire, J.-C. Beugnot, and L. Thévenaz, “Analytical modeling of the gas-filling dynamics in photonic crystal fibers”, *Applied Optics* **49**, 4604–4609 (2010).

- [66] M. Bouchiat, J. Guéna, P. Jacquier, M. Lintz, and A. Papoyan, “Electrical conductivity of glass and sapphire cells exposed to dry cesium vapor”, *Applied Physics B* **68**, 1109–1116 (1999).
- [67] J. Crank, *The mathematics of diffusion*, 2nd ed. (Clarendon Press, 1975).
- [68] P. Clausing, “Über die Adsorptionszeit und ihre Messung durch Strömungsversuche”, *Annalen der Physik* **399**, 489–520 (1930).
- [69] H. De Freitas, M. Oria, and M. Chevrollier, “Spectroscopy of cesium atoms adsorbing and desorbing at a dielectric surface”, *Applied Physics B* **75**, 703–709 (2002).
- [70] A. Urvoy, *Set-up of a laser system for precision spectroscopy of highly excited caesium atoms*, Diploma thesis, Universität Stuttgart, 5. Physikalisches Institut, 2011.
- [71] C. Milstead and L. Zumwalt, “Cesium deposition on stainless steel”, *Nuclear Technology* **3**, 495–499 (1967).
- [72] A. D. Slepko, A. R. Bhagwat, V. Venkataraman, P. Londero, and A. L. Gaeta, “Diffusion and redistribution of rubidium in hollow-core photonic bandgap fibers”, in *International quantum electronics conference* (Optical Society of America, 2009), p. IMC2.
- [73] S. Bennett, J. Roberts, and C. Wieman, “Measurement of the dc Stark shift of the $6S \rightarrow 7S$ transition in atomic cesium”, *Physical Review A* **59**, R16 (1999).
- [74] G. Dattoli, L. Giannessi, L. Mezi, and A. Torre, “Theory of generalized Bessel functions”, *Il Nuovo Cimento B Series 11* **105**, 327–348 (1990).
- [75] M. Bason, “Coherent atom-light interactions in multi-level systems”, PhD thesis (Durham University, 2009).
- [76] F. A. Tauschinsky, “Rydberg atoms on a chip and in a cell”, PhD thesis (University of Amsterdam, 2013).
- [77] A. D. Slepko, A. R. Bhagwat, V. Venkataraman, P. Londero, and A. L. Gaeta, “Generation of large alkali vapor densities inside bare hollow-core photonic band-gap fibers”, *Optics Express* **16**, 18976–18983 (2008).
- [78] H. Tyagi, H. Lee, P. Uebel, M. Schmidt, N. Joly, M. Scharrer, and P. S. J. Russell, “Plasmon resonances on gold nanowires directly drawn in a step-index fiber”, *Optics Letters* **35**, 2573–2575 (2010).
- [79] C. M. Cordeiro, C. J. de Matos, E. M. dos Santos, A. Bozolan, J. S. Ong, T. Facincani, G. Chesini, A. R. Vaz, and C. H. B. Cruz, “Towards practical liquid and gas sensing with photonic crystal fibres: side access to the fibre microstructure and single-mode liquid-core fibre”, *Measurement Science and Technology* **18**, 3075 (2007).
- [80] C. Hensley, D. H. Broaddus, C. B. Schaffer, and A. L. Gaeta, “Photonic band-gap fiber gas cell fabricated using femtosecond micromachining”, *Optics Express* **15**, 6690–6695 (2007).
- [81] M. Fleischhauer, A. Imamoglu, and J. P. Marangos, “Electromagnetically induced transparency: optics in coherent media”, *Reviews of Modern Physics* **77**, 633 (2005).
- [82] A. Vasilyev, I. Savukov, M. Safronova, and H. Berry, “Measurement of the $6s$ - $7p$ transition probabilities in atomic cesium and a revised value for the weak charge Q_W ”, *Physical Review A* **66**, 020101 (2002).

Danksagung

An dieser Stelle möchte ich mich bei allen bedanken, die diese Arbeit möglich gemacht haben. Ohne die Unterstützung meiner Betreuer, wissenschaftlichen Mitstreiter, Familie und Freunde wäre das Experiment Masterarbeit sicherlich nicht gelungen.

Prof. Dr. Tilman Pfau danke ich nicht nur für die Möglichkeit am Institut mitzuarbeiten, sondern auch für die Ermöglichung eines Auslandsaufenthaltes in Toronto und für eine begeisterte Vorlesung, die mich bereits vor meinem Bachelorabschluss zur Atomphysik brachte.

Bei Prof. Dr. Martin Dressel möchte ich mich für die Übernahme des Mitberichts und für die Unterhaltung im Rahmen des Zwischenberichts bedanken.

Bei Robert Löw, dem geistigen Vater des Experiments, möchte ich mich recht herzlich für das Vertrauen bedanken das er mir entgegenbrachte, als er mir das Projekt übertrug und dafür, dass er immer Zeit für mich fand. Ohne ihn hätte es nie eine „Ofenkartoffel“ gegeben.

Georg danke ich nicht nur für die Betreuung während meiner Arbeit, sondern auch für einen sehr inspirierenden Ausflug zum Max-Planck-Institut in Erlangen, der mit dem Besuch der Kulturstätte „Berch“ verbunden war.

Die tolle Atmosphäre am Institut ist allen Mitarbeitern zu verdanken. Insbesondere bedanke ich mich bei dem Team aus dem dritten Stock, das mir stets mit Rat und Tat zur Seite stand. Harald, Georg und Robert möchte ich zudem für das Korrekturlesen von Teilen dieses Schriftstücks danken.

Axel, der inzwischen in der Elektronikwerkstatt anzutreffen ist, danke ich für sehr erhellende Diskussionen. Wer weiß, ob die Atome in den Fasern ohne seine Expertise je eine Radiowelle hätten erleben dürfen.

Bei Gabriele Untereiner vom 1. Physikalischen Institut möchte ich mich herzlich für das Aufdampfen meiner Kondensatorplatten bedanken.

Tobias, Matthias und Philipp bin ich sehr dankbar für die gemeinsame Zeit im Studium. Das gemeinsam Erlebte, ob an der Universität oder außerhalb, möchte ich nicht missen.

Bei Sarah möchte ich mich nicht nur über so manche Anmerkung zur englischen Sprache bedanken, sondern auch für die gemütlichen Feierabendbiere, die mich dazu brachten das Labor zu verlassen und Atome Atome sein zu lassen.

Meiner Familie bin ich sehr dankbar dafür, dass sie immer für mich da war und mich stets dabei unterstützt hat Physik zu studieren.